iScience

CellPress

Article

Synthetic Route to a Triphenylenehexaselenol-Based Metal Organic Framework with Semi-conductive and Glassy Magnetic Properties

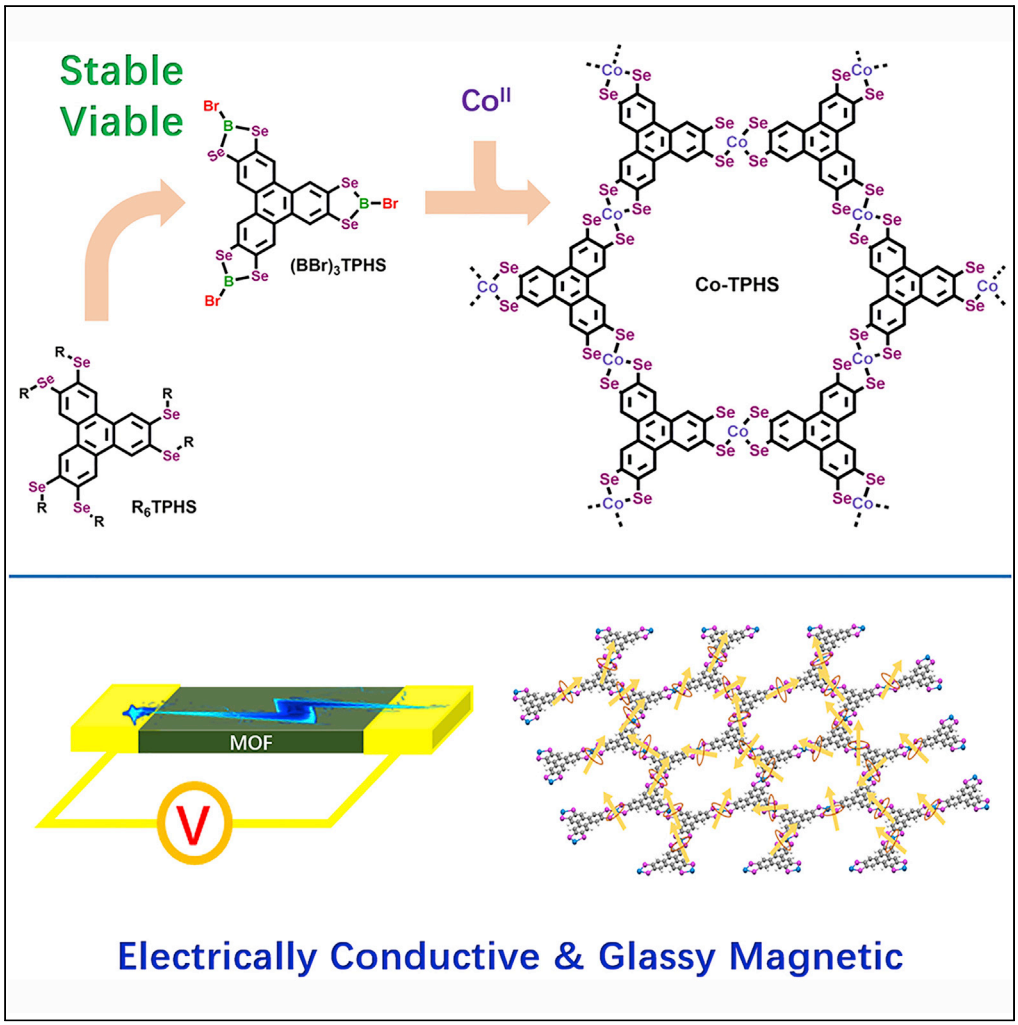

Yutao Cui, Jie Yan, Zhijun Chen, ..., Caiming Liu, Wei Xu, Daoben Zhu

cmliu@iccas.ac.cn (C.L.)
wxu@iccas.ac.cn (W.X.)

HIGHLIGHTS

A BBr_3-induced dealkylation protocol is used to synthesize arenepolyselenols ligands

Triphenylenehexaselenol (TPHS) and a Co-TPHS MOF were synthesized for the first time

The MOF exhibits electrically conductive and glassy magnetic properties

Cui et al., iScience 23, 100812
January 24, 2020
https://doi.org/10.1016/j.isci.2019.100812

iScience

CellPress

Article

Synthetic Route to a Triphenylenehexaselenol-Based Metal Organic Framework with Semi-conductive and Glassy Magnetic Properties

Yutao Cui,[1,2] Jie Yan,[1,2] Zhijun Chen,[1,2] Weilong Xing,[1,2] Chunhui Ye,[1,2] Xiang Li,[3] Ye Zou,[1,2] Yimeng Sun,[1] Caiming Liu,[1,2,*] Wei Xu,[1,2,4,*] and Daoben Zhu[1,2]

SUMMARY

In the latest decade, two-dimensional (2D) π-d conjugated metal organic frameworks (MOFs) constructed from metal ions with square-planar coordination geometry and benzene- or triphenylene-derived ligands with ortho-disubstituted N, O, or S donor atoms have received great research interests because of their exceptional physical properties and promising applications. New MOFs of this class are constantly being reported, but 2D metal bis(diselenolene) MOFs based on organic ligands with ortho-disubstituted Se donor atoms have not been synthesized. Herein, a Lewis-acid-induced dealkylation protocol is introduced to the synthesis of arenepolyselenols and related coordination polymers. A triphenylene-derived diselenaborole compound is synthesized and employed as precursor reagent for the synthesis of 2,3,6,7,10,11-triphenylenehexaselenol (H_6TPHS) and the first conductive metal organic framework namely Co-TPHS based on triphenylenehexaselenolate ($TPHS^{6-}$). Co-TPHS exhibits porous honeycomb 2D structure and electrically conductive and glassy magnetic properties.

INTRODUCTION

Two dimensional (2D) π-d conjugated metal organic frameworks (MOFs) perform exceptional electrically conductive properties and potential applications in electronics (Sun et al., 2016; Stassen et al., 2017; Ko et al., 2018; Zhao et al., 2018). The structurally related 2D MOFs are made from π-conjugated planer ligands and single metal ion with square-planar coordinative geometry (Sun et al., 2016; Ko et al., 2018). The in-planer π-d conjunction, in favors of charge carriers' delocalization, leads to exceptional electrical conductivity different from traditional MOFs. Due to their intrinsic electrical conductivity and porosity, conductive MOFs in this class exhibit promising applications in electrocatalysis, transparent electrodes, energy storage, and chemoreceptive sensors (Campbell et al., 2015; Dong et al., 2015; Feng et al., 2018; Huang et al., 2017, 2018; Jin et al., 2017; Li et al., 2017; Miner et al., 2016, 2017, 2018; Park et al., 2018b; Sheberla et al., 2017; Smith et al., 2016; Wu et al., 2017). As bottom-up fabricated solid materials, MOFs with tunable structures and different properties are mainly defined by the two building blocks: metal centers and organic ligands. Up to now, a series of benzene-, triphenylene-, coronene-, or phthalocyanine-derived π-conjugated ligands with different donor atoms (O, S, and N) have been employed for the construction of π-d conjugated MOFs with metal bis(dithiolene), metal catecholates, metal bis(diaminoene) and metal bis(aminothiolato) units (Kambe et al., 2013, 2014; Huang et al., 2015; Pal et al., 2015; Clough et al., 2017; Dong et al., 2018a, 2018b; Sheberla et al., 2014; Dou et al., 2017; Lahiri et al., 2017; Hmadeh et al., 2012; Park et al., 2018a; Meng et al., 2019; Yang et al., 2019; Zhong et al., 2019). Theoretical studies indicate that replacing sulfur by selenium in a hybrid organic–inorganic semiconductor is predicted to decrease the electronic band gap (Stott et al., 2012). Although the synthesis of the protected benzenepolyselenols has been reported, metal bis(diselenolene) 2D MOFs have not been synthesized and reported up to now (Turner and Vaid, 2012; Stott et al., 2012). Synthesis of arenepolyselenols and MOFs based on these ligands is significant for the research of structure-property relationship on the conductive MOFs, as well as providing diversity of conductive 2D materials for further studies on physical properties and electronic applications.

Arene(polysthiols), as arene(polyselenols) analogous, are frequently prepared via reductive cleavage of arenepoly(alkylthioethers) under Birch conditions using alkali metal in liquid ammonia (Figure S1). The starting arenepoly(alkylthioethers) are commonly synthesized via the nucleophilic aromatic substitution

[1]Beijing National Laboratory for Molecular Sciences, Key Laboratory of Organic Solids, Institute of Chemistry, Chinese Academy of Sciences, Beijing 100190, China

[2]University of Chinese Academy of Sciences, Beijing 100049, China

[3]Institute of Chemistry, Chinese Academy of Sciences, Beijing 100190, China

[4]Lead Contact

*Correspondence: cmliu@iccas.ac.cn (C.L.), wxu@iccas.ac.cn (W.X.)

https://doi.org/10.1016/j.isci.2019.100812

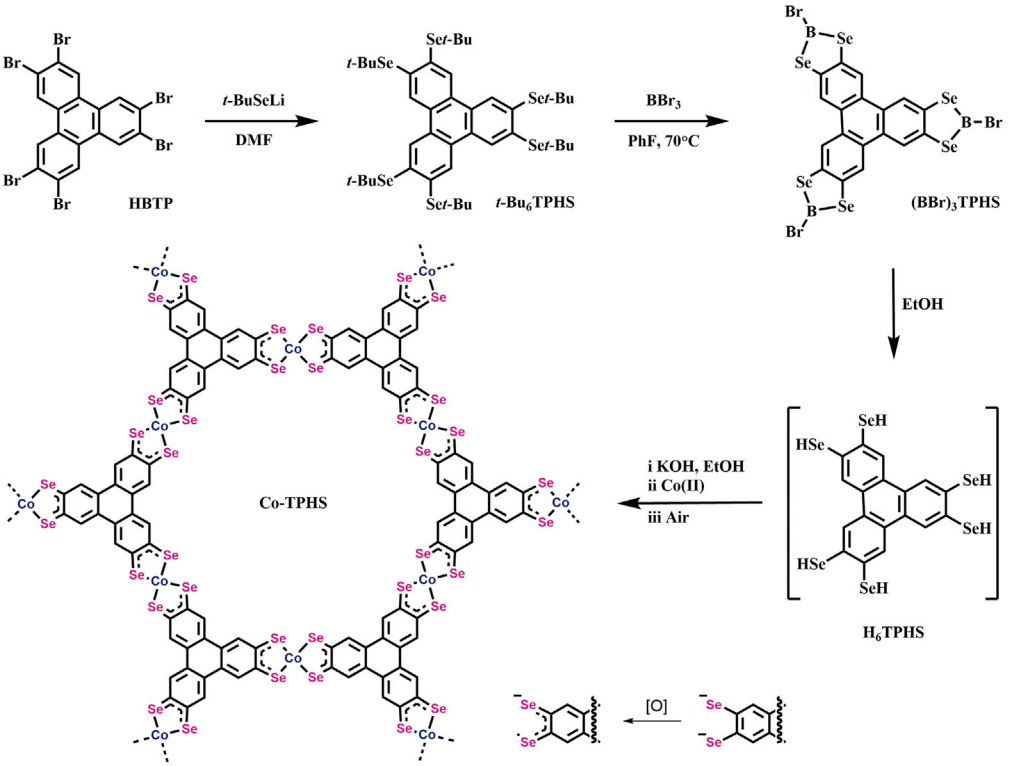

Figure 1. Synthetic Route of H_6TPHS and Co-TPHS

of arene(polyhalides) with alkylthiolates. An analogous route was applied to the synthesis of two acetyl-protected benzene(polyselenols) (Turner and Vaid, 2012). As arene(polyselenols) are air-sensitive, it is difficult to obtain arene(polyselenols) in the form of selenol. An alternative route (Figure S2) to arene(polyselenols) is the Lewis-acid-promoted dealkylation of arenepoly(alkylselenoethers). A Lewis-acid (BBr_3)-induced deprotection procedure has been applied in the production of 2-bromobenzo-1,3,2-dithiaboroles (Schlindwein et al., 2016). We introduce the Lewis-acid-induced deprotection protocol to the synthesis of arene(polyselenols). The resulting diselenaboroles are available as precursor for the synthesis of arene(polyselenols) and related MOFs. Recently, we have successfully synthesized the ligand benzenehexaselenol (H_6BHS) via the method of boron tribromide as Lewis acid to promote the reproduction of the alkyl benzene-polyselenols (Cui et al., 2019). Here we report the first synthesis of selenium-substituted triphenylene ligand 2,3,6,7,10,11-triphenylenehexaselenol (H_6TPHS) and the first member of 2D MOFs based on triphenylenehexaselenolate namely Co-TPHS.

RESULTS AND DISCUSSION

Synthesis

As illustrated in Figure 1, the MOF Co-TPHS was synthesized by the coordination reaction of 2,3,6,7,10,11-triphenylenehexa(selenolate) ($(TPHS)^{6-}$) and cobaltous ions in the presence of base. Under inert atmosphere, the as-prepared $(BBr)_3$TPHS was treated with ethyl alcohol and potassium hydroxide and stirred for a while. During which, $(TPHS)^{6-}$ was formed. Then cobaltous salt was added and the reaction mixture was heated to reflux and stirred for 24h. The as-made MOF is air sensitive. The color of the MOF turned from green to black-green in about twenty seconds following the exposure to air (Figure S3), indicating the oxidation of Co-TPHS. The reaction mixture was stirred under air for 12h to ensure the complete oxidization of the as-made MOF. Then the material Co-TPHS ($Co_{1.5}$(TPHS)) was yielded as bulk black-green powder. It is noteworthy that the addition of base and getting the reaction temperature reaching reflux temperature of ethyl alcohol are critical to obtain samples with high crystallinity.

To understand the synthetic process, model reactions aiming at benzene-1,2,4,5-tetraselenol (H_4BTS) and a reported coordination polymer Co-BTS were carried (Figure 2). (Turner and Vaid, 2012; Downes and

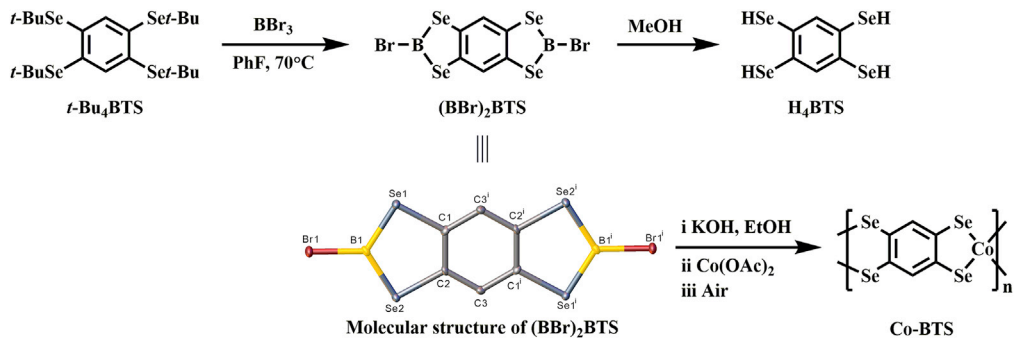

Figure 2. Synthesis of Benzene-1,2,4,5-tetraselenol (H_4BTS) and 1D Coordination Polymer Co-BTS and Molecular Structure of $(BBr)_2BTS$

Marinescu, 2017) The corresponding diselenaboroles $(BBr)_2BTS$ was synthesized via the BBr_3-promoted cleavage of protected alkyl groups. A solution of 1,2,4,5-benzenetetra(selenolate) ($(BTS)^{4-}$) in D_2O was prepared by treating the diselenaborole compound with $LiOD/D_2O$ for the NMR characterization. The H^1NMR and C^{13}NMR spectrum (Figures S25 and S26) showed reasonable peaks corresponding to $Li_4C_6H_2Se_4$. As good solubility of $(BBr)_2BTS$ in hot PhF, single-crystals of $(BBr)_2BTS$ were obtained via slowly cooling a hot solution of $(BBr)_2BTS$ in PhF. And as shown in Figure S4 and Table S1, the structure was further confirmed via single-crystal X-ray diffraction. The expected five-member cyclic 2-bromo-1,3,2-diselenaboroles were observed. The organic ligand benzene-1,2,4,5-tetraselenol (H_4BTS) was generated in good yield by methanolysis of $(BBr)_2BTS$. It's the first time that the molecule H_4BTS is obtained in the form of benzeneselenol. It is noteworthy that the ligand H_4BTS is unstable and just can be exposed to air for a while and stored under argon atmosphere for about three days. The one-dimensional coordination polymer namely Co-BTS was synthesized by the coordination reaction of cobaltous ions and $(BTS)^{4-}$, which was generated *in situ* via treating the diselenaborole compound with a solution of KOH in alcohol solvents. The structural characterization results are consistent with that of Co-BTS in reported literature previously (presented in Supplemental Information, Figures S5 and S6).

Structural Resolution

Powder X-ray diffraction (PXRD) measurements reveal a layered structure of Co-TPHS with honeycomb lattice, which is similar to the MOFs constructed from triphenylene-derived ligands. As showed in Figure 3, the prominent diffraction peaks at $2\theta = 4.3°$ and 8.8°, corresponding to the [100] and [200] reflections, indicate long-range order within the ab plane. The 100 spacing is ~20.5Å. The weak and broad peak at $2\theta = \sim 27°$, corresponding the [001] reflection, indicates poor coherence along the c direction or a small dimension along the c-axis in the Co-TPHS crystallites. The interspace of 001 crystal face is ~3.3Å. To determine the staking arrangement of the 2D sheets, we simulated two possible eclipsed (AA) and slipped-parallel (AB) staking patterns. As the limitation of the few numbers of diffraction peaks in experimental PXRD patterns and the similar PXRD patterns simulated from the AA and AB models, it is difficult to determine the accurate stacking geometry. Both the positions and intensity profile of the PXRD calculated from the AA staking are more consistent with the experimental data than that of AB staking. The cell parameters calculated from the AA stacking (a = 23.718Å, b = 23.718Å, c = 3.400Å, $\alpha = 90°$, $\beta = 90°$, $\gamma = 120°$ in P 6/mmm space group) are consistent with the experimental result of Co-TPHS.

A distinct flaky morphology of Co-TPHS was observed in the scanning electron microscopy (SEM) photos. As shown in Figure S7, Co-TPHS is composed of nanosheets with the size varying from several tens to more than three hundreds of nanometers in diameter and about ten nanometers in thickness. The arrangement of the nanosheets is irregular and incompact. Transmission electron microscopy (TEM) images were also obtained to further confirm the structure of Co-TPHS (Figure 4). Irregularly arranged nanosheets were observed and uniform honeycomb lattice with d_{100} = ~20Å was shown in the nanosheet (along [001]) just in parallel with the observation plane, which is consistent with the 2D honeycomb model obtained from PXRD results (d_{100} = 20.5Å). The elemental mapping shows homogeneous distribution of Co, Se, and C (Figure S8).

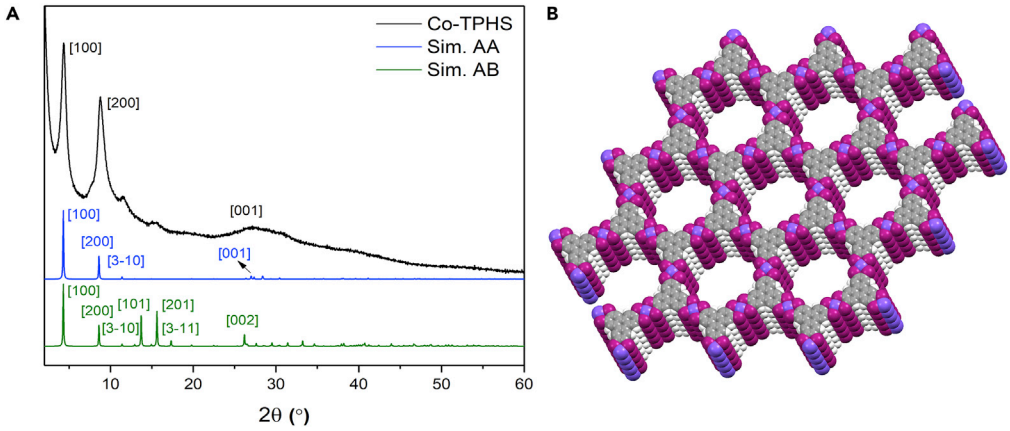

Figure 3. PXRD Analysis and Simulated Structure of Co-TPHS

(A) A comparison of the PXRD of the Co-TPHS and simulated patterns of structure models with AA and AB stacking patterns.

(B) Illustration of the 2D lattice of Co-TPHS.

As shown in Figure S9, the porous character of Co-TPHS was revealed in N_2 sorption experiments (at 77 K). The Brunauer–Emmett–Teller (BET) surface area of Co-TPHS is 246 m^2 g^{-1}, and the surface area data are comparable to catecholate and dithiolene systems that also build upon the triphenylene core.

Component Analysis

The electron probe microanalysis (EPMA) results of Co-TPHS indicate the existence of cobalt, selenium, and carbon, and the calculated atom ratio of selenium to cobalt is ~4.0 (or 6:1.51). The molecular formula of Co-TPHS is $Co_{1.5}(C_{18}H_6Se_6)$ according to the EPMA result. The content of C was analyzed by elemental analysis (EA). The weight percentage of carbon was determined to be 27.22%, which are coincident with the calculated result (27.56%) of the formula of $Co_{1.5}(C_{18}H_6Se_6)$, showing that the cobalt bis(diselenolene) unit was oxidized to be electroneutral. Most of the reported MOFs that exhibit staked honeycomb lattices and are made from triphenylene-derived ligands with ortho-disubstituted S, O, or N donor atoms and square-planar coordination late-transition-metals are expected to be oxidized to be electroneutral (Sun et al., 2016).

X-ray photoelectron spectroscopy (XPS) experiments were performed for further characterization of the MOFs. As showed in Figure S10, the full XPS spectrum reveals the presence of C, Se, and Co. In the Co 2p region (Figure S11A), two peaks at binding energies of 778.5 and 793.6 eV correspond to the 2p3/2 and 2p1/2. Two corresponding satellite peaks locate at the higher-binding energy side, which signifies a +2 oxidation state on Co. The XPS result of Co 2p suggests no electron transfer between metal ions and organic ligands. And the oxidation of Co-TPHS by air occurred on the organic ligands, which was oxidized to be $TPHS^{(3-)\ (3\bullet)}$ to achieve charge balance with Co^{2+}. In the Se 3d region (Figure S11B), two dominating peaks located at binding energies of 778.5 and 793.6 eV are observed for 3d5/2 and 3d3/2, in agreement with those of previously reported metal-diselenolene polymers (Downes and Marinescu, 2017; Cui et al., 2018).

Electrical Conductivity

The electrical conductivity (σ) of Co-TPHS was measured on the pressed pellet sample via a standard two-probe method. The σ of Co-TPHS reaches 10^{-6} S cm^{-1} at 300 K. As shown in Figure 5, temperature dependence of electrical conductivity reveals typically semi-conductive behavior of Co-TPHS. The electrical conductivity increases with the elevated temperature and reaches 10^{-5} S cm^{-1} at 400 K. The ligands with stable radicals provide unpaired electrons as charge carriers. The in-planer π-d conjunction, in favors of charge carriers' delocalization, provide through bonds pathway for charge transport. The activation energy (Ea) of electrical conductivity can be estimated by fitting the temperature-dependent electrical conductivities to the Arrhenius equation (Givaja et al., 2012). Figure S12A shows the linear plot of natural logarithm of conductivity (ln σ) versus the reciprocal of the absolute temperature (1/T). The slope of the curve can be

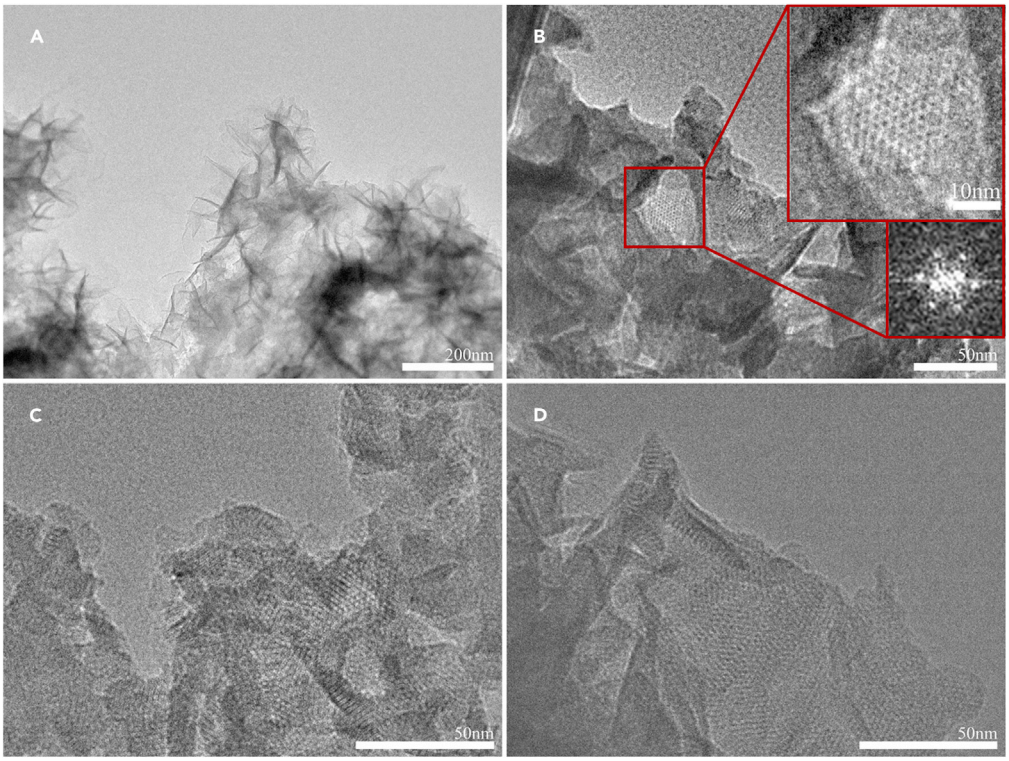

Figure 4. TEM Images of the Co-TPHS

(A–D) TEM images of the Co-TPHS nanosheets at different magnifications. The insets of Figure B are larger version of the red highlighted region (top and right) and the fast Fourier transform of the image (middle and right).

seen as -Ea/k (k = Boltzmann constant). The Ea of Co-TPHS is estimated to be 294 meV. As shown in Figure S12B, the linear dependence of ln σ versus $T^{-1/4}$ indicates that charge carrier transport in Co-TPHS sample is well fitted to the three-dimensional variable range hopping (3D-VRH) model. The optical band gap of Co-TPHS was confirmed to be 2.33 eV. Bulk Co-TPHS is a wide-band semiconductor.

Band structure of monolayer of the 2D lattice and eclipsed AA stacking bulk crystal are calculated by using the plane-wave technique as implemented in CASTEP code (Figures S13 and S14). The valence and conducting band of monolayer structure show relatively narrow dispersing comparing with that of the previously reported 2D MOFs based on BHT(benzenehexathiol) and TPHT (triphenylenehexathiol), indicating the weaker electronic coupling between the d-orbital of Co ion and π-orbital of the ligand. The calculated band gap is much smaller compared with what is observed in the optical spectroscopy. This might attribute to the fact that the band gaps are usually underestimated in the DFT calculations. The influences of the existence of defects and uncertainty of the edge structure have not been addressed in the theoretical calculation yet. The absorption observed in optical spectroscopy may come from the defects and few layer nanostructures of this 2D MOF, which should be different from what expected for an ideal bulk crystal. And the metal organic coordination solid might be doped by defects or uncompleted oxidization sites (Co-TPHS was oxidized to be electroneutral by air), both of which will influence the band structure diverging from theoretical calculation. The bulk crystal shows a highly dispersed band structure with bandwidth over 2 eV in the valence band, which indicates the strong interlayer electronic couplings between this 2D lattices. With the Fermi energy crossing the highly dispersed valence band, large charge carrier density as well as high carrier mobility should be expected. But only poor electrical conductivity can be observed. Considering the weak and broad [001] peak at $2\theta = \sim 27°$, which refers poor coherence along the c direction or a small dimension along the c-axis, indicating that the material obtained is not a real bulk crystal, especially in the stacking direction. It is more like a nanosheet containing only a few layers of the 2D lattice, in which the electrical transport behavior is obviously different from a real bulk material.

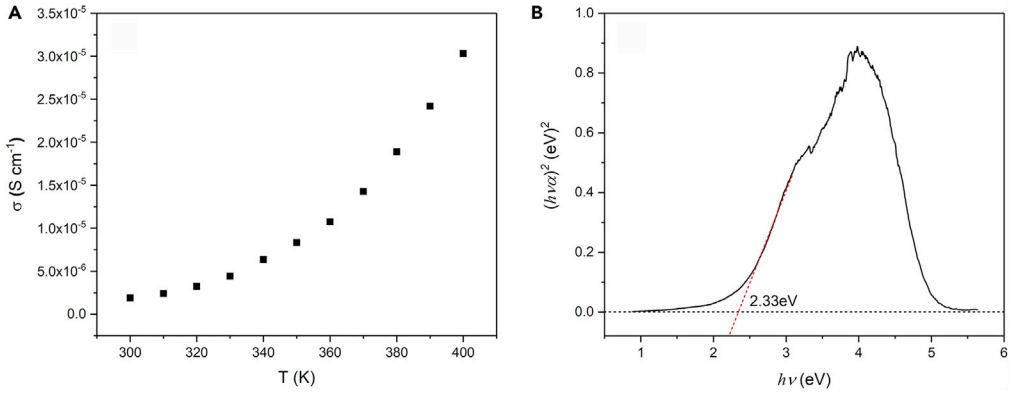

Figure 5. Electrically Conductive Properties of Co-TPHS

(A) Temperature dependence of electrical conductivity of Co-TPHS.

(B) Tauc plots of $(\alpha h\nu)^2$ versus photon energy ($h\nu$) for Co-TPHS. A linear fit (red line) was used to estimate the band gap by extrapolating to zero absorption.

Magnetism

DC magnetic susceptibility is measured in a 1000 Oe field and a 2-300K temperature range. As shown in Figure 6A, the room temperature χT value of 2.764 cm^3 K mol^{-1} is consist with the value of 2.625 cm^3 K mol^{-1} expected for one spin-only Co^{2+} cations (S = 3/2, assuming g = 2.0) and 2/3 ligand of $TPHS^{(3-)\ (3\bullet)}$. The χT value decreases slowly with decreasing temperature, indicating the existence of weak intramolecular antiferromagnetic exchange. The $1/\chi$ data above 100 K is in line with the Curie-Weiss law well, with the θ value of −14.48 K and the C value of 5.33 cm^3 K mol^{-1} (Figure S15). After reaching a minimum value of 1.99 cm^3 K mol^{-1} at 44 K, the χT value suddenly increases sharply to the maximum value of 6.50 cm^3 K mol^{-1} at 7 K, indicating the occurrence of magnetic phase transition. The χT product drops sharply when it is less than 7 K, which may be caused by Zero field splitting, Zeeman effect, and/or weak interlayer antiferromagnetic interactions.

The zero-field cooling (ZFC) and the field cooling (FC) magnetic susceptibility divergence appear below about 3.6 K (Figure 6B), indicating that magnetization irreversibility occurs. Alternating-current (ac) magnetic susceptibility investigation reveals that both the in-phase component (χ') and the out-of-phase component (χ'') of Co-TPHS are frequency dependent (Figure 6C). These phenomena indicate that each magnetic moment is frozen at low temperatures, which are characteristic of spin-glass or single-molecule magnets (Liu et al., 2008). In order to determine whether it is spin-glass or single-molecule magnet, a parameter, $\Phi = (\Delta T_p/T_p)/\Delta(\log f)$ (Mydosh, 1993), in which T_p and f are the peak temperature and the frequency, respectively, must be introduced. The Φ value of Co-TPHS is calculated to be 0.081; this value is more consistent with the behavior of the spin-glass ($\approx$0.01) but smaller than single-molecule magnet ($\geq$0.1) (Mydosh, 1993). A small hysteresis can be clearly observed at 1.9 K of Co-TPHS (Figure 6D), with a coercive field (H_c) of 160 Oe. Furthermore, the field-dependent magnetization at 2 K for Co-TPHS (Figure S16) reveals that only a low magnetization value of 0.86 Nβ is observed even at the highest field measured (50 kOe), and saturation cannot occur, which is consistent with weak ferromagnetism owing to glassy magnet. Such glassiness might result from the not necessarily homogeneous topology of Co-TPHS (Jeon Ie et al., 2015). The oxidation of Co-TPHS might introduce defects to the as-made Cp-TPHS. What is more, the existence of two types of spin carrier (Co^{2+} and $TPHS^{(3-)\ (3\bullet)}$) in Co-TPHS leads to complicated magnetism.

Conclusion

In conclusion, the H_6TPHS and 2D conductive MOFs Co-TPHS were synthesized for the first time. A novel Lewis-acid-induced dealkylation protocol was applied for the synthesis of a TPHS-derived diselenaborole, which was used as a precursor reagent for the preparation of H_6TPHS. Co-TPHS was synthesized via simple homogeneous reaction. Co-TPHS is composed of nanosheets with honeycomb lattice and exhibit porous, electrically conductive, and magnetic properties. The synthesis of H_6TPHS and Co-TPHS verify an easy

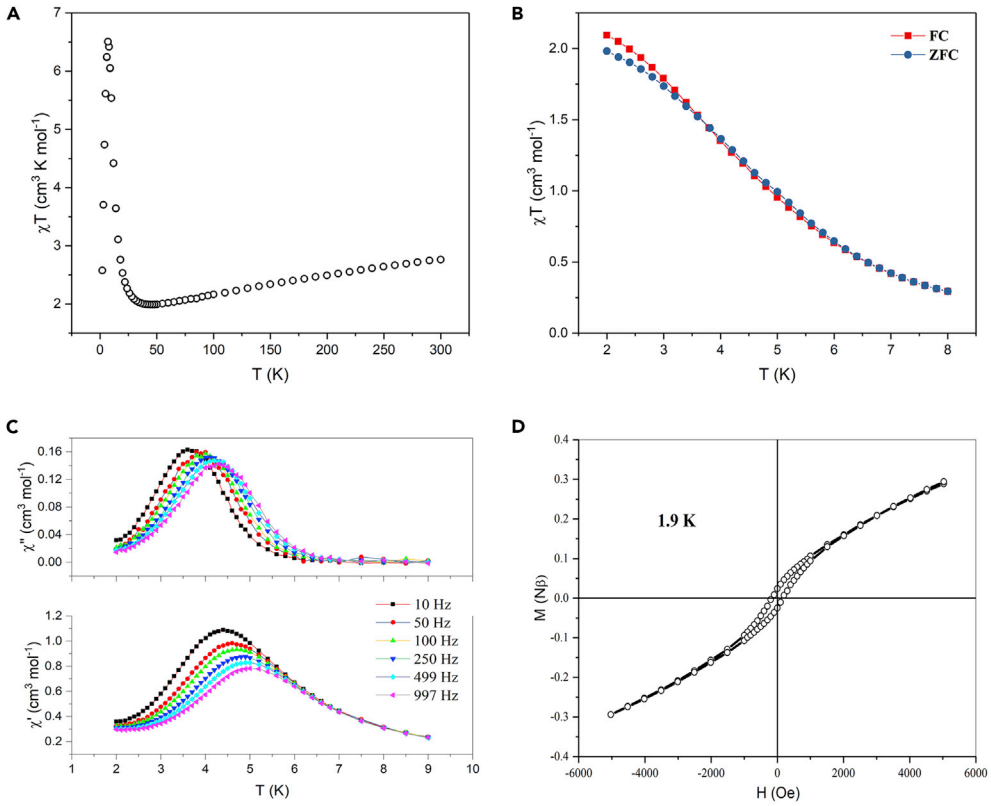

Figure 6. Magnetic Properties of Co-TPHS

(A) Plot of χT versus T of Co-TPHS under 1k Oe field.

(B) Plots of FC and ZFC susceptibilities vs. temperature of Co-TPHS at an applied field of 30 Oe.

(C) Ac susceptibilities of Co-TPHS measured in an ac field of 2.5 Oe.

(D) Hysteresis loop at 2.0 (K).

route to arenepolyselenols ligand and metal bis(diselenolene) MOFs, simultaneously providing new materials for the study of further applications and structure-property relationship.

METHODS

All methods can be found in the accompanying Transparent Methods supplemental file.

SUPPLEMENTAL INFORMATION

Supplemental Information can be found online at https://doi.org/10.1016/j.isci.2019.100812.

ACKNOWLEDGMENTS

We gratefully acknowledge the financial support from the National Key R&D Program of China (Grant No. 2017YFA0204701), the Chinese Academy of Sciences (Strategic Priority Research Program No. XDB12000000, QYZDY-SSW-SLH024), and National Natural Science Foundation of China (21333011, 21661132006, 21790051, 51403215).

AUTHOR CONTRIBUTIONS

D.Z. and W.X. initiated and supervised the research program. Y.C. Z. C. and C. Y. were responsible for the material preparation and characterizations. W-L. X. and Y. Z. collected and analyzed X-ray photoelectron spectroscopy data. Y. C. and Y. S. collected and analyzed electrical conductivity data. C. L. performed the measurement magnetic properties. J. Y. and X. L. carried out the TEM measurement. Y. C., C. L.,

and W. X. wrote the manuscript. All the authors participated in the discussion and interpretation of data, read the manuscript, and provided input.

DECLARATION OF INTERESTS

The authors declare no competing interests.

Received: May 17, 2019
Revised: September 3, 2019
Accepted: December 23, 2019
Published: January 24, 2020

REFERENCES

Campbell, M.G., Sheberla, D., Liu, S.F., Swager, T.M., and Dinca, M. (2015). Cu(3)(hexaiminotriphenylene)(2): an electrically conductive 2D metal-organic framework for chemiresistive sensing. Angew. Chem. Int. Ed. *54*, 4349–4352.

Clough, A.J., Skelton, J.M., Downes, C.A., de la Rosa, A.A., Yoo, J.W., Walsh, A., Melot, B.C., and Marinescu, S.C. (2017). Metallic conductivity in a two-dimensional cobalt dithiolene metal-organic framework. J. Am. Chem. Soc. *139*, 10863–10867.

Cui, Y., Yan, J., Chen, Z., Zhang, J., Zou, Y., Sun, Y., Xu, W., and Zhu, D. (2019). [Cu3(C6Se6)]n: the first highly conductive 2D π-d conjugated coordination polymer based on benzenehexaselenolate. Adv. Sci. *6*, 1802235.

Cui, Y., Yan, J., Sun, Y., Zou, Y., Sun, Y., Xu, W., and Zhu, D. (2018). Thermoelectric properties of metal-(Z)-1,2-dihydroselenoethene-1,2-dithiol coordination polymers. Sci. Bull. *63*, 814–816.

Dong, R., Han, P., Arora, H., Ballabio, M., Karakus, M., Zhang, Z., Shekhar, C., Adler, P., Petkov, P.S., Erbe, A., et al. (2018a). High-mobility band-like charge transport in a semiconducting two-dimensional metal-organic framework. Nat. Mater. *17*, 1027–1032.

Dong, R., Pfeffermann, M., Liang, H., Zheng, Z., Zhu, X., Zhang, J., and Feng, X. (2015). Large-area, free-standing, two-dimensional supramolecular polymer single-layer sheets for highly efficient electrocatalytic hydrogen evolution. Angew. Chem. Int. Ed. *54*, 12058–12063.

Dong, R., Zhang, Z., Tranca, D.C., Zhou, S., Wang, M., Adler, P., Liao, Z., Liu, F., Sun, Y., Shi, W., et al. (2018b). A coronene-based semiconducting two-dimensional metal-organic framework with ferromagnetic behavior. Nat. Commun. *9*, 2637.

Dou, J.H., Sun, L., Ge, Y., Li, W., Hendon, C.H., Li, J., Gul, S., Yano, J., Stach, E.A., and Dinca, M. (2017). Signature of metallic behavior in the metal-organic frameworks M3(hexaiminobenzene)2 (M = Ni, Cu). J. Am. Chem. Soc. *139*, 13608–13611.

Downes, C.A., and Marinescu, S.C. (2017). Bioinspired metal selenolate polymers with tunable mechanistic pathways for efficient H2 evolution. ACS Catal. *7*, 848–854.

Feng, D., Lei, T., Lukatskaya, M.R., Park, J., Huang, Z., Lee, M., Shaw, L., Chen, S., Yakovenko, A.A., Kulkarni, A., et al. (2018). Robust and conductive two-dimensional metal−organic frameworks with exceptionally high volumetric and areal capacitance. Nat. Energy *3*, 30–36.

Givaja, G., Amo-Ochoa, P., Gomez-Garcia, C.J., and Zamora, F. (2012). Electrical conductive coordination polymers. Chem. Soc. Rev. *41*, 115–147.

Hmadeh, M., Lu, Z., Liu, Z., Gándara, F., Furukawa, H., Wan, S., Augustyn, V., Chang, R., Liao, L., Zhou, F., et al. (2012). New porous crystals of extended metal-catecholates. Chem. Mater. *24*, 3511–3513.

Huang, X., Sheng, P., Tu, Z., Zhang, F., Wang, J., Geng, H., Zou, Y., Di, C.A., Yi, Y., Sun, Y., et al. (2015). A two-dimensional pi-d conjugated coordination polymer with extremely high electrical conductivity and ambipolar transport behaviour. Nat. Commun. *6*, 7408.

Huang, X., Yao, H., Cui, Y., Hao, W., Zhu, J., Xu, W., and Zhu, D. (2017). Conductive copper benzenehexathiol coordination polymer as a hydrogen evolution catalyst. ACS Appl. Mater. Interfaces *9*, 40752–40759.

Huang, X., Zhang, S., Liu, L., Yu, L., Chen, G., Xu, W., and Zhu, D. (2018). Superconductivity in a copper(II)-Based coordination polymer with perfect kagome structure. Angew. Chem. Int. Ed. *57*, 146–150.

Jeon Ie, R., Negru, B., Van Duyne, R.P., and Harris, T.D. (2015). A 2D semiquinone radical-containing microporous magnet with solvent-induced switching from Tc = 26 to 80 K. J. Am. Chem. Soc. *137*, 15699–15702.

Jin, Z., Yan, J., Huang, X., Xu, W., Yang, S., Zhu, D., and Wang, J. (2017). Solution-processed transparent coordination polymer electrode for photovoltaic solar cells. Nano Energy *40*, 376–381.

Kambe, T., Sakamoto, R., Hoshiko, K., Takada, K., Miyachi, M., Ryu, J.H., Sasaki, S., Kim, J., Nakazato, K., Takata, M., and Nishihara, H. (2013). pi-Conjugated nickel bis(dithiolene) complex nanosheet. J. Am. Chem. Soc. *135*, 2462–2465.

Kambe, T., Sakamoto, R., Kusamoto, T., Pal, T., Fukui, N., Hoshiko, K., Shimojima, T., Wang, Z., Hirahara, T., Ishizaka, K., et al. (2014). Redox control and high conductivity of nickel bis(dithiolene) complex pi-nanosheet: a potential organic two-dimensional topological insulator. J. Am. Chem. Soc. *136*, 14357–14360.

Ko, M., Mendecki, L., and Mirica, K.A. (2018). Conductive two-dimensional metal-organic frameworks as multifunctional materials. Chem. Commun. (Camb.) *54*, 7873–7891.

Lahiri, N., Lotfizadeh, N., Tsuchikawa, R., Deshpande, V.V., and Louie, J. (2017). Hexaaminobenzene as a building block for a family of 2D coordination polymers. J. Am. Chem. Soc. *139*, 19–22.

Li, W.-H., Ding, K., Tian, H.-R., Yao, M.-S., Nath, B., Deng, W.-H., Wang, Y., and Xu, G. (2017). Conductive metal-organic framework nanowire array electrodes for high-performance solid-state supercapacitors. Adv. Funct. Mater. *27*, 1702067.

Liu, C.-M., Zhang, D.-Q., and Zhu, D.-B. (2008). Solvatomagnetic effect and spin-glass behavior in a 1D coordination polymer constructed from EE-azido bridged MnIII3O units. Chem. Commun. (Camb.), 368–370.

Meng, Z., Aykanat, A., and Mirica, K.A. (2019). Welding metallophthalocyanines into bimetallic molecular meshes for ultrasensitive, low-power chemiresistive detection of gases. J. Am. Chem. Soc. *141*, 2046–2053.

Miner, E.M., Fukushima, T., Sheberla, D., Sun, L., Surendranath, Y., and Dinca, M. (2016). Electrochemical oxygen reduction catalysed by Ni3(hexaiminotriphenylene)2. Nat. Commun. *7*, 10942.

Miner, E.M., Gul, S., Ricke, N.D., Pastor, E., Yano, J., Yachandra, V.K., Van Voorhis, T., and Dincă, M. (2017). Mechanistic evidence for ligand-centered electrocatalytic oxygen reduction with the conductive MOF Ni3(hexaiminotriphenylene)2. ACS Catal. *7*, 7726–7731.

Miner, E.M., Wang, L., and Dincă, M. (2018). Modular O2 electroreduction activity in triphenylene-based metal–organic frameworks. Chem. Sci. *9*, 6286–6291.

Mydosh, J.A. (1993). Spin Glasses, an Experimental Introduction (Taylor and Francis Ltd).

Pal, T., Kambe, T., Kusamoto, T., Foo, M.L., Matsuoka, R., Sakamoto, R., and Nishihara, H. (2015). Interfacial synthesis of electrically conducting palladium bis(dithiolene) complex nanosheet. ChemPlusChem *80*, 1255–1258.

Park, J., Hinckley, A.C., Huang, Z., Feng, D., Yakovenko, A.A., Lee, M., Chen, S., Zou, X., and Bao, Z. (2018a). Synthetic routes for a 2D

semiconductive copper hexahydroxybenzene metal-organic framework. J. Am. Chem. Soc. *140*, 14533–14537.

Park, J., Lee, M., Feng, D., Huang, Z., Hinckley, A.C., Yakovenko, A., Zou, X., Cui, Y., and Bao, Z. (2018b). Stabilization of hexaaminobenzene in a 2D conductive metal-organic framework for high power sodium storage. J. Am. Chem. Soc. *140*, 10315–10323.

Schlindwein, S.H., Bader, K., Sibold, C., Frey, W., Neugebauer, P., Orlita, M., Slageren, J., and Gudat, D. (2016). New selective synthesis of dithiaboroles as a viable pathway to functionalized benzenedithiolenes and their complexes. Inorg. Chem. *55*, 6186–6194.

Sheberla, D., Bachman, J.C., Elias, J.S., Sun, C.J., Shao-Horn, Y., and Dinca, M. (2017). Conductive MOF electrodes for stable supercapacitors with high areal capacitance. Nat. Mater. *16*, 220–224.

Sheberla, D., Sun, L., Blood-Forsythe, M.A., Er, S., Wade, C.R., Brozek, C.K., Aspuru-Guzik, A., and Dinca, M. (2014). High electrical conductivity in Ni(3)(2,3,6,7,10,11-hexaiminotriphenylene)(2), a semiconducting metal-organic graphene analogue. J. Am. Chem. Soc. *136*, 8859–8862.

Smith, M.K., Jensen, K.E., Pivak, P.A., and Mirica, K.A. (2016). Direct self-assembly of conductive nanorods of metal–organic frameworks into chemiresistive devices on shrinkable polymer films. Chem. Mater. *28*, 5264–5268.

Stassen, I., Burtch, N., Talin, A., Falcaro, P., Allendorf, M., and Ameloot, R. (2017). An updated roadmap for the integration of metal-organic frameworks with electronic devices and chemical sensors. Chem. Soc. Rev. *46*, 3185–3241.

Stott, A.C., Vaid, T.P., Bylaska, E.J., and Dixon, D.A. (2012). Tuning band gap energies in Pb3(C6X6) extended solid-state structures. J. Phys. Chem. C *116*, 8370–8378.

Sun, L., Campbell, M.G., and Dinca, M. (2016). Electrically conductive porous metal-organic frameworks. Angew. Chem. Int. Ed. *55*, 3566–3579.

Turner, D.L., and Vaid, T.P. (2012). Synthesis of protected benzenepolyselenols. J. Org. Chem. *77*, 9397–9400.

Wu, G., Huang, J., Zang, Y., He, J., and Xu, G. (2017). Porous field-effect transistors based on a semiconductive metal-organic framework. J. Am. Chem. Soc. *139*, 1360–1363.

Yang, C., Dong, R., Wang, M., Petkov, P.S., Zhang, Z., Wang, M., Han, P., Ballabio, M., Brauninger, S.A., Liao, Z., et al. (2019). A semiconducting layered metal-organic framework magnet. Nat. Commun. *10*, 3260.

Zhao, M., Huang, Y., Peng, Y., Huang, Z., Ma, Q., and Zhang, H. (2018). Two-dimensional metal-organic framework nanosheets: synthesis and applications. Chem. Soc. Rev. *47*, 6267–6295.

Zhong, H., Ly, K.H., Wang, M., Krupskaya, Y., Han, X., Zhang, J., Zhang, J., Kataev, V., Buchner, B., Weidinger, I.M., et al. (2019). A phthalocyanine-based layered two-dimensional conjugated metal-organic framework as a highly efficient electrocatalyst for the oxygen reduction reaction. Angew. Chem. Int. Ed. *58*, 10677–10682.

ISCI, Volume *23*

Supplemental Information

Synthetic Route to a Triphenylenehexaselenol-Based Metal Organic Framework with Semi-conductive and Glassy Magnetic Properties

Yutao Cui, Jie Yan, Zhijun Chen, Weilong Xing, Chunhui Ye, Xiang Li, Ye Zou, Yimeng Sun, Caiming Liu, Wei Xu, and Daoben Zhu

Synthetic route to a triphenylenehexaselenol based metal organic framework with semi-conductive and glassy magnetic properties

Yutao Cui[1,2], Jie Yan[1,2], Zhijun Chen[1,2], Weilong Xing[1,2], Chunhui Ye[1,2], Xiang Li[3], Ye Zou[1,2], Yimeng Sun[1], Caiming Liu[1,2*], Wei Xu[1,2*], and Daoben Zhu[1,2].

1 Beijing National Laboratory for Molecular Sciences, Key Laboratory of Organic Solids, Institute of Chemistry, Chinese Academy of Sciences, Beijing 100190, China

2 University of Chinese Academy of Sciences, Beijing 100049, China.

3 Institute of Chemistry, Chinese Academy of Sciences, Beijing 100190, China

SUPPORTING INFORMATION

Table of Contents

TRANSPARENT METHODS P1

General remark P1

Synthesis P1

Characterization P2

Figure S1. The most commonly synthetic route to arenepolythiols. P2

Figure S2. The postulated reaction mechanism for the dealkylation of bis(tert-butylselanyl)-benzene according to a reported literature. P2

Figure S3. Molecular structures of $(BBr)_2BTS$ (top) and the photo of crystalline $(BBr)_2BTS$ (bottom). P3

Table S1. Color contrast of Co-TPHS in inert atmosphere and after exposed to air. P3

Figure S4. Crystal data and structure refinement for $(BBr)_2BTS$. P3

Figure S5. XPS analysis of Co-BTS. P5

Figure S6. N_2 sorption isotherms at 77 K for Co-TPHS. P5

Figure S7. Temperature dependence of electrical conductivity of Co-BTS. P6

Figure S8. Elements mapping of Co-TPHS. P6

Figure S9. SEM images of Co-TPHS. P7

Figure S10. Full XPS spectra of Co-TPHS. P7

Figure S11. XPS analysis of Co-TPHS. (a) Co 2p and (b) Se 3d. P8

Figure S12. a) Plots of lnσ versus 1/T of Co-TPHS. b) Dependence of lnσ versus $T^{-1/4}$. P8

Figure S13. Band structure and density of state (DOS) of the monolayer of Co-TPHS complex calculated at PBE level. K point Γ=(0,0,0); K=(-0.333,0.667,0.000); M=(0.000,0.500,0.000). The Fermi level is at zero. P8

Figure S14. Band structure of the bulk crystal of eclipsed AA stacking Co-TPHS complex calculated at PBE level. K point Γ=(0,0,0); A=(0.000,0.000,0.500); H=(0.333,0.667,0.500); K=(-0.333,0.667,0.000); M=(0.000,0.500,0.000); L=(0.000,0.500,0.500). The Fermi level is at zero. P9

Figure S15. The field dependent magnetization at 2 K for Co-TPHS. P9

Figure S16. Plot of χ^{-1} versus T of Co-TPHS under 1k Oe field. P10

Figure S17. TGA curves of Co-TPHS. P10

Figure S18. PXRD patterns of Co-TPHS after the treatment in different thermal or chemical environment for 24h. P11

Figure S19. ^{1}H-NMR (400MHz, 298K, $CDCl_3$) spectrum of $(t\text{-Bu})_6$TPHS. P12

Figure S20. ^{13}C-NMR (400MHz, 298K, $CDCl_3$) spectrum of $(t\text{-Bu})_6$TPHS. P12

Figure S21. ^{1}H-NMR (400MHz, 298K, LiOD/D_2O) spectrum of $(Li)_6$TPHS which was obtained from the reaction of $(BBr)_3$TPHS and LiOD in D_2O. P13

Figure S22. ^{13}C-NMR (400MHz, 298K, LiOD/D_2O) spectrum of $(Li)_6$TPHS which was obtained from the reaction of $(BBr)_3$TPHS and LiOD in D_2O. P13

Figure S23. ^{1}H-NMR (400MHz, 298K, $CDCl_3$) spectrum of $(BBr)_2BTS$. P14

Figure S24. ^{13}C-NMR (400MHz, 298K, $CDCl_3$) spectrum of $(BBr)_2BTS$. P14

Figure S25. ^{1}H-NMR (400MHz, 298K, LiOD/D_2O) spectrum of $(Li)_4BTS$ which was obtained from the reaction of $(BBr)_2BTS$ and LiOD in D_2O. P15

Figure S26. ^{13}C-NMR (400MHz, 298K, LiOD/D_2O) spectrum of $(Li)_4BTS$ which was obtained from the reaction of $(BBr)_2BTS$ and LiOD in D_2O. P15

Figure S27. ^{1}H-NMR (400MHz, 298K, $CDCl_3$) spectrum of H_4BTS. P16

SUPPORTING INFORMATION

Figure S28. ^{13}C-NMR (400MHz, 298K, $CDCl_3$) spectrum of H_4BTS. **P16**

References **P17**

SUPPORTING INFORMATION

TRANSPARENT METHODS

General remark:

2,3,6,7,10,11-hexabromotriphenylene HBTP was synthesized by a reported literature method.(Yatabe et al., 2000) Selenium powder (325 mesh) and KOH were purchased from Alfa Aesar and used as received. Boron tribromide, tert-Butyllithium (1.3M solution in pentane), cobalt(II) acetate tetrahydrate and fluorobenzene were purchased from J&K and used as received. The extra dry solvents tetrahydrofuran (THF), N, N-Dimethylformamide (DMF) and ethyl alcohol were purchased from Acros Organics. The degasification of solvents was conducted through freeze-pump-thaw cycling.

Synthesis:

(*t*-Bu)$_4$BTS was synthesized according a reported literature method.(Turner and Vaid, 2012) (*t*-Bu)$_6$TPHS was synthesized by similar method (1.5 equiv of *t*-BuSeLi per functional group). The two compounds were characterized via NMR analysis.

(*t*-Bu)$_4$BTS: ^{1}H NMR (400 MHz, $CDCl_3$) δ 8.11 (s, 2H), 1.49 (s, 36H). ^{13}C NMR (400 MHz, $CDCl_3$) δ 145.44, 137.52, 45.84, 32.56. (Figure S23 and S24)

(*t*-Bu)$_6$TPHS: ^{1}H NMR (400 MHz, $CDCl_3$) δ 8.94 (s, 6H), 1.55 (s, 54H). ^{13}C NMR (400 MHz, $CDCl_3$) δ 137.69, 132.30, 128.91, 45.83, 32.46. (Figure S19 and S20)

(BBr)$_3$TPHS: Under argon atmosphere, (*t*-Bu)$_6$TPHS (1.04g, 1mmol) was dissolved in fluorobenzene (60ml), then BBr_3 (1.53g, 6mmol) was added. The stirred resulting mixture was heated at 70℃ for 12h. During which, a lightly yellow precipitate formed. Then the reaction mixture was cooled to rt. The precipitate was filtered off and washed with hexane. The solid production was used for the next reaction as soon as possible and without further treatment. As the poor solubility and sensitive B-Br bond, it's difficulty to do characterization of (BBr)$_3$TPHS directly. (BBr)$_3$TPHS was dissolved in a degassed solution of LiOD in D_2O (5% w/w) to produce a solution of $TPHS^{6-}$, which is used for NMR characterization. [$C_{18}H_6Se_6Li_6$] ^{1}H NMR (400 MHz, LiOD/D_2O) δ 8.42 (s, 6H). ^{13}C NMR (400 MHz, LiOD/D_2O) δ 142.40, 128.18, 124.00. (Figure S21 and S22)

Co-TPHS: Under argon atmosphere, freshly prepared (BBr)$_3$TPHS (0.4mmol) was dispersed in degassed ethyl alcohol (60ml) by ultrasonic for about 30 seconds. Then KOH (348mg. 6mmol) was added and stirred for 10min at rt. During which, the yellow suspended particulate dissolved to form a light green solution and then yellow solid precipitate out. $Co(OAc)_2$•$4H_2O$ (150mg, 0.6mmol) was added to the stirred reaction solution and a green precipitate formed. The reaction mixture was heated to reflux and stirred for 24h, and then cooled to rt. The suspension was exposed to air and the color of the suspended solid turned from green to black-green. The reaction mixture was stirred under air for 12h. The precipitated product was filtered off and washed with distilled water, methanol, dichloromethane and ether thoroughly. The final product Co-TPHS was obtained as black-green powder after drying under vacuum at 100℃ for 12 hours. Co-TPHS exhibits good thermal and chemical stability (Figure S17 and S18).

(BBr)$_2$BTS: Under argon atmosphere, (*t*-Bu)$_4$BTS (1.04g, 1mmol) was dissolved in fluorobenzene (60ml), then BBr_3 (1.53g, 6mmol) was added. The resulting mixture was stirred for 12h at 70℃, allowed to cool to rt. The precipitate was filtered off and washed with hexane. The solid production was used for the next reaction as soon as possible and without further treatment. (BBr)$_2$BTS was dissolved in a degassed solution of LiOD in D_2O (5% w/w) to produce a solution of BTS^{4-}, which is used for NMR characterization. [$C_6H_2Se_4Li_4$] ^{1}H NMR (400 MHz, LiOD/D_2O) δ 7.48 (s, 2H). ^{13}C NMR (400 MHz, LiOD/D_2O) δ 142.55, 134.27. (Figure S25 and S26)

(BBr)$_2$BTS (single crystals): Under argon atmosphere, (*t*-Bu)$_4$BTS (100mg, 1mmol) was dissolved in fluorobenzene (60ml), then BBr_3 (1.53g, 6mmol) was added. The resulting mixture was stirred for 12h at 70℃. The resulting clear yellow solution was kept without disturbance, allowed to cool to rt slowly, and stored at rt for overnight. Yellow needle-like crystals with 1-2cm in length and ~1mm in diameter were generated.

Co-BTS: Under argon atmosphere, freshly prepared (BBr)$_2$BTS (1mmol) was dispersed in degassed ethyl alcohol (60ml) by ultrasonic for about 30 seconds. Then KOH (348mg. 6mmol) was added and stirred for 10min at rt. $Co(OAc)_2$•$6H_2O$ (250mg, 1mmol) was added to the stirred reaction solution and a black precipitate formed. The reaction mixture was heated to reflux and stirred for 24h, and then cooled to rt. The suspension was exposed to air and stirred under air for 12h. The precipitated was filtered off and washed with distilled water, methanol, dichloromethane and ether thoroughly. The final product Co-BTS was obtained as black powder after drying under vacuum at 100℃ for 12 hours.

H_4BTS: Under argon atmosphere, (BBr)$_2$BTS (1mmol) was dispersed in degassed ethyl alcohol (50ml). The resulting mixture was stirred for 10min at rt. The precipitate was filtered off, washed with degassed ethyl alcohol and without further purification. The final product H_4BTS was obtained as light-yellow powder after drying under vacuum at rt for 2 hours. ^{1}H NMR (400 MHz, $CDCl_3$) δ 7.68 (s, 2H), 2.01 (s, 4H). ^{13}C NMR (400 MHz, $CDCl_3$) δ 138.09, 129.17. (Figure S27 and S28) Anal. Calcd for $C_6H_6Se_4$: C, 18.29; H, 1.54; N, 0.00. Found: C, 18.53; H, 1.42; N, <0.30.

SUPPORTING INFORMATION

Characterization

The content of C and H was analyzed by a Flash EA 1112 (Thermo Fisher Scientific). The content of Cu, and Se was carried on inductively coupled plasma optical emission spectrometer (Optima 5300DV, Perkin Elmer). ^{13}C-NMR spectra of *t*-Bu$_6$BHS was recorded at 500 MHz (Bruker) and other NMR spectra was recorded at 400 MHz (Bruker). The chemical shifts were reported in parts per million (ppm) using the residual solvent signals as internal standards. Powder X-ray diffraction (PXRD) patterns were obtained at a PANalytical Empyrean II X-Ray diffractometer using Cu Ka irradiation (λ=1.5406 Å). XPS and UPS were performed by using AXIS Ultra-DLD ultrahigh vacuum photoemission spectroscopy system (Kratos Co.). A monochromatic magnesium Ka source (1253.8 eV) and a He I source (21.11 eV) were used for XPS and UPS, respectively. And Cu-BHS powder and a pressed pellet (thickness = ~0.05mm) were used for XPS and UPS measurements, respectively. The IR spectrum of Cu-BHS was obtained at a TENSOR-27 spectrometer (Bruker). Thermogravimetric analysis (TGA) was performed on a PerkinElmer TGA 8000 instrument under nitrogen atmosphere. The materials were compressed into cuboid pellets (5mm×10mm×~0.1mm) under a pressure of 10 MPa to measure the electrical conductivity. The temperature-dependent electrical conductivity was measured using two-contact probe method on the pressed pellets by using a KEITHLEY 2002 Multimeter (Keithley Instrument Inc.).

The magnetic susceptibility measurements were performed in a commercial Quantum Design MPMS-XL5 SQUID magnetometer. Diamagnetic corrections were applied using Pascal's constants for all constituent atoms.

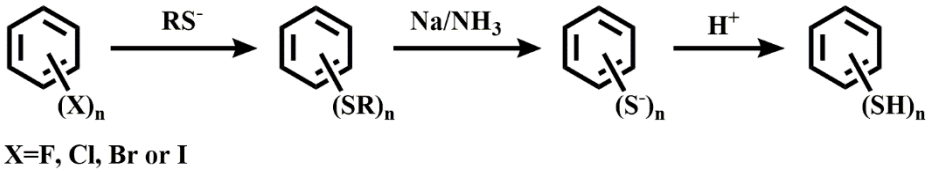

Figure S1. The most commonly synthetic route to arenepolythiols. (related to Figure 1)

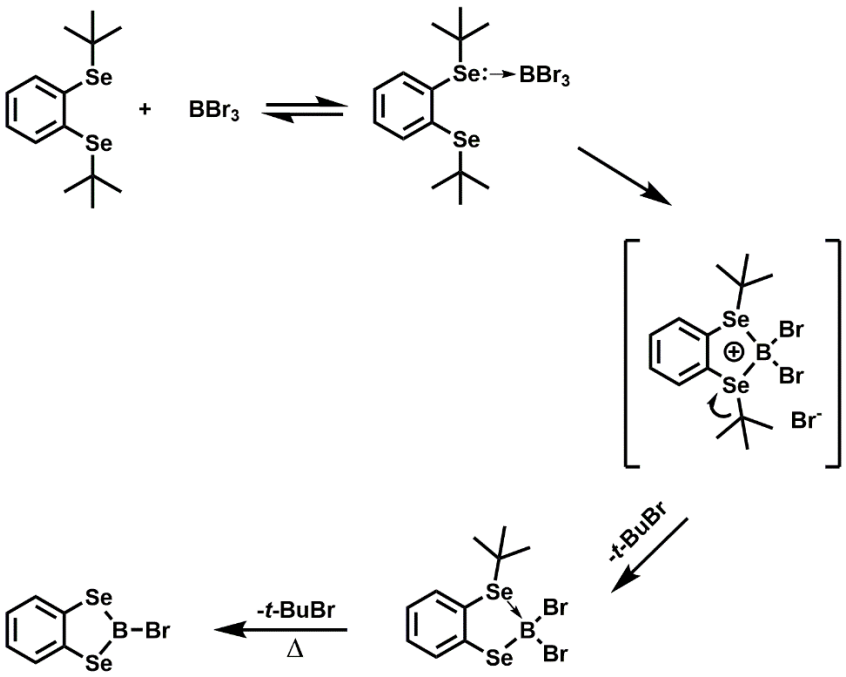

Figure S2. The postulated reaction mechanism for the dealkylation of bis(tert-butylselanyl)benzene according to a reported literature. (related to Figure 1)

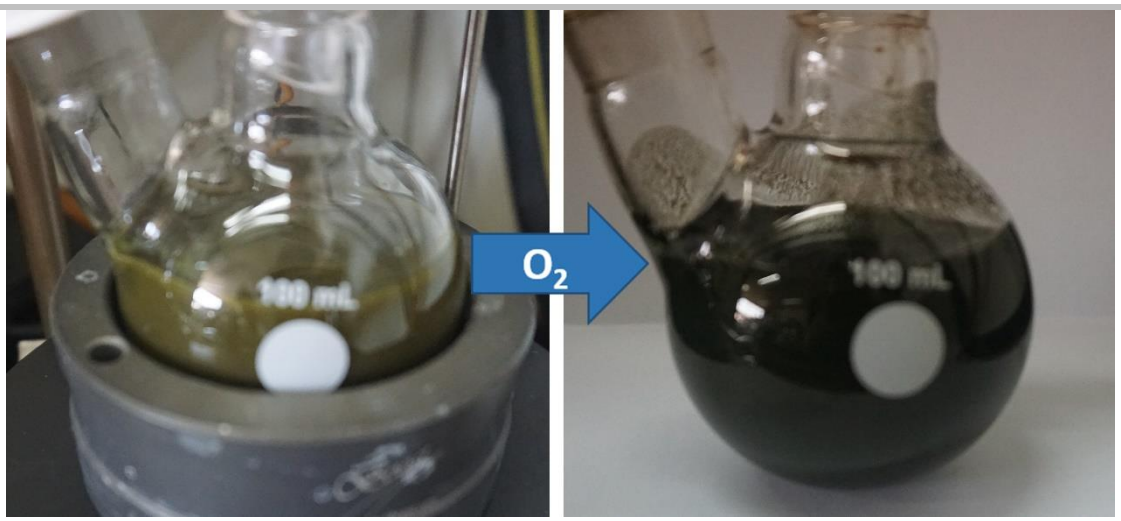

Figure S3. Color contrast of Co-TPHS in inert atmosphere and after exposed to air. (related to Figure 1)

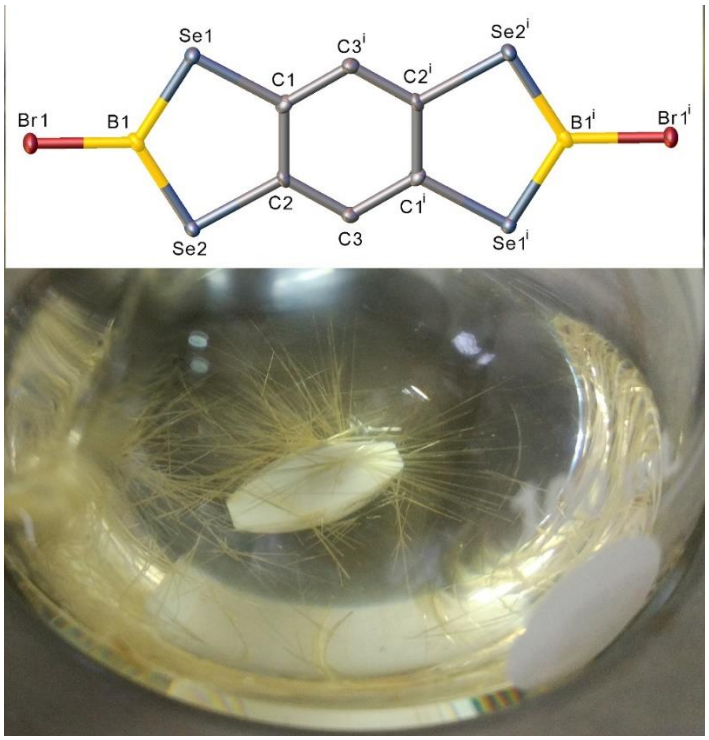

Figure S4. Molecular structures of $(BBr)_2BTS$ (top) and the photo of crystalline $(BBr)_2BTS$ (bottom). (related to Figure 2)

Table S1. Crystal data and structure refinement for $(BBr)_2BTS$. (related to Figure 2)

Empirical formula	$C_6H_2B_2Br_2Se_4$	
Formula weight	571.36	
Temperature	173.15 K	
Wavelength	0.71073 Å	
Crystal system	Triclinic	
Space group	P-1	
Unit cell dimensions	a = 4.137(3) Å	α= 98.53(2)°.
	b = 11.636(9) Å	β= 99.12(2)°.

	c = 12.733(8) Å	γ = 93.44(2)°.
Volume	596.3(7) $Å^3$	
Z	2	
Density (calculated)	3.182 Mg/m^3	
Absorption coefficient	18.957 mm^{-1}	
F(000)	508	
Crystal size	0.289 x 0.143 x 0.064 mm^3	
Theta range for data collection	1.641 to 27.502°.	
Index ranges	-5<=h<=5, -15<=k<=15, -16<=l<=16	
Reflections collected	2719	
Independent reflections	2719 [R(int) = ?]	
Completeness to theta = 25.242°	99.7 %	
Absorption correction	Semi-empirical from equivalents	
Max. and min. transmission	1.00000 and 0.24762	
Refinement method	Full-matrix least-squares on F^2	
Data / restraints / parameters	2719 / 0 / 128	
Goodness-of-fit on F^2	1.109	
Final R indices [I>2sigma(I)]	R1 = 0.0418, wR2 = 0.1037	
R indices (all data)	R1 = 0.0453, wR2 = 0.1064	
Extinction coefficient	n/a	
Largest diff. peak and hole	0.837 and -0.902 $e.Å^{-3}$	

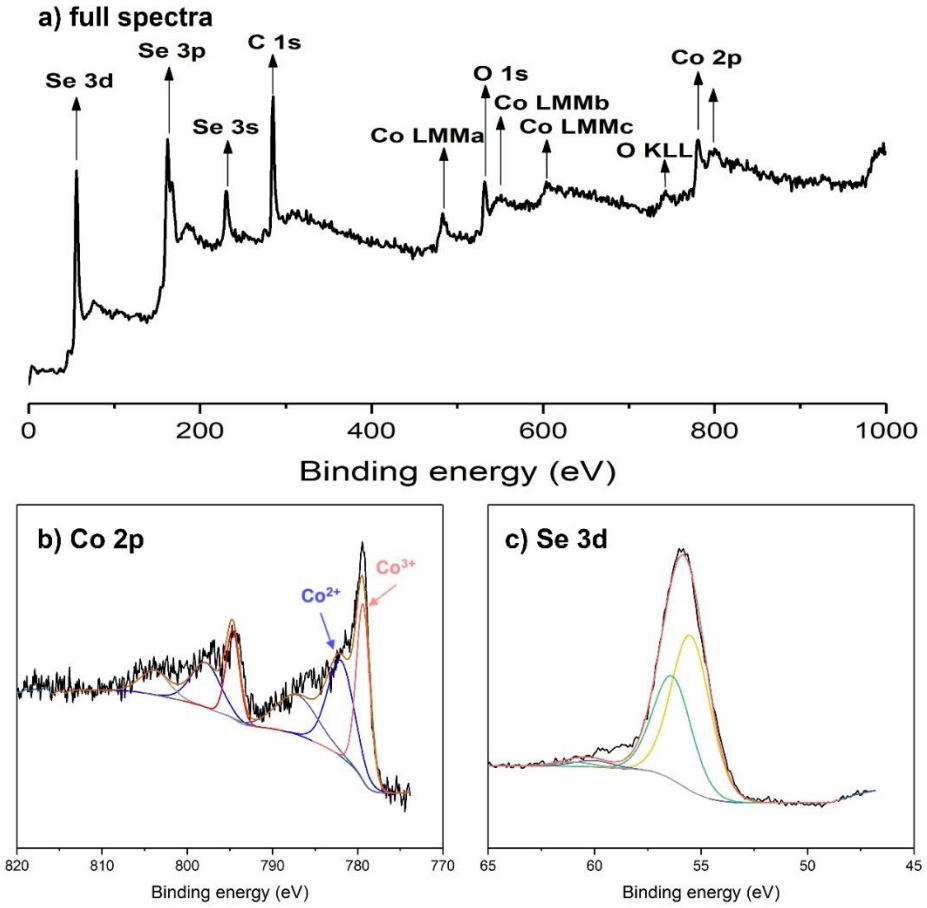

Figure S5. XPS analysis of Co-BTS. The exitance of Co^{3+} might result from charge transfer between organic ligands and Co ions, suggesting stronger π–d interaction among the ladder coordination polymer. (related to Figure 2)

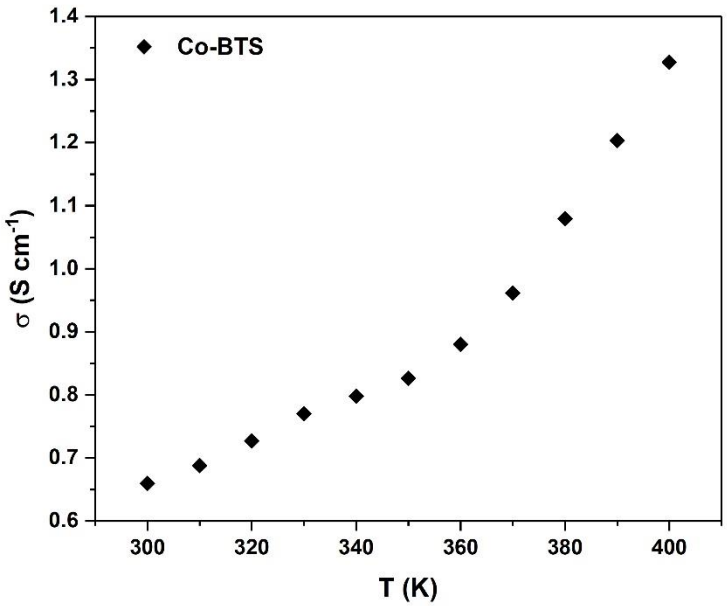

Figure S6. Temperature dependence of electrical conductivity of Co-BTS (pressed pellet, four probes). The conductivity of Co-BTS reaches ~0.6 S cm^{-1} at 300K. (related to Figure 2)

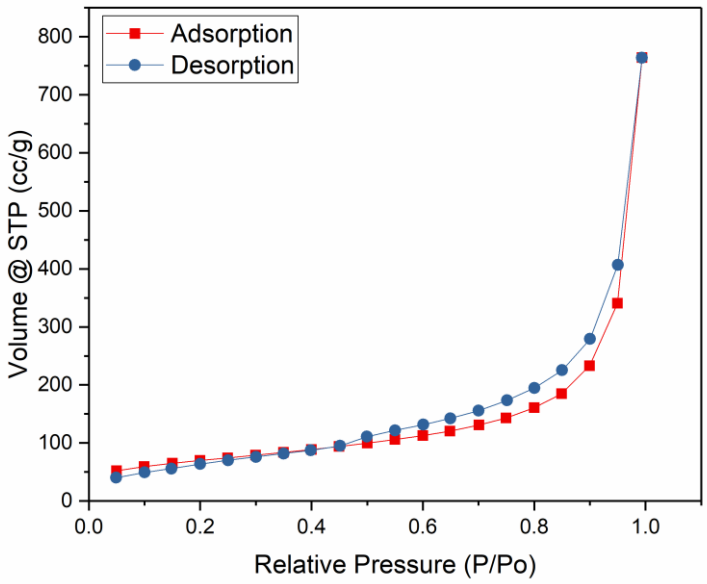

Figure S7. N_2 sorption isotherms at 77 K for Co-TPHS. (related to Figure 3)

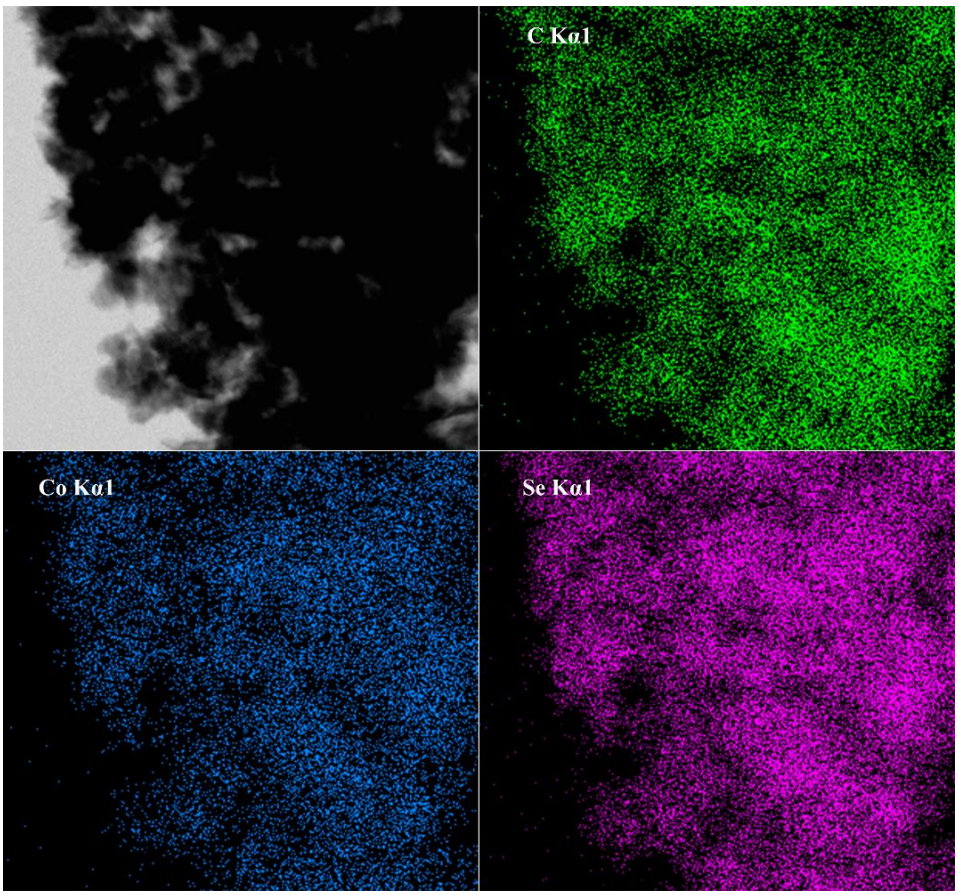

Figure S8. Elements mapping of Co-TPHS. (related to Figure 3)

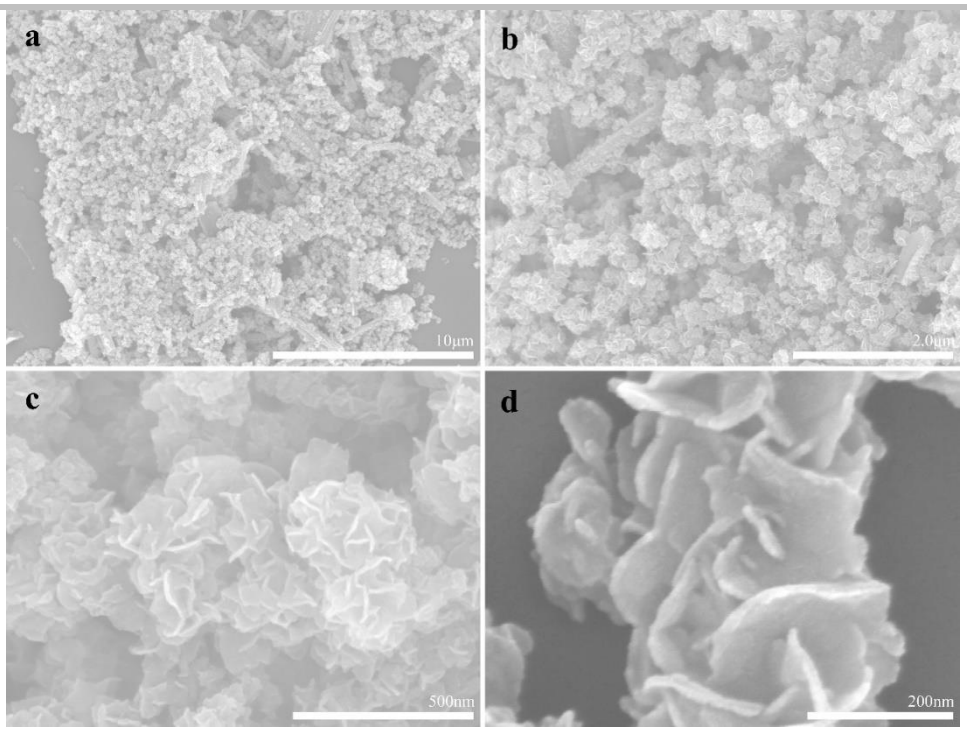

Figure S9. SEM images of Co-TPHS. (related to Figure 3)

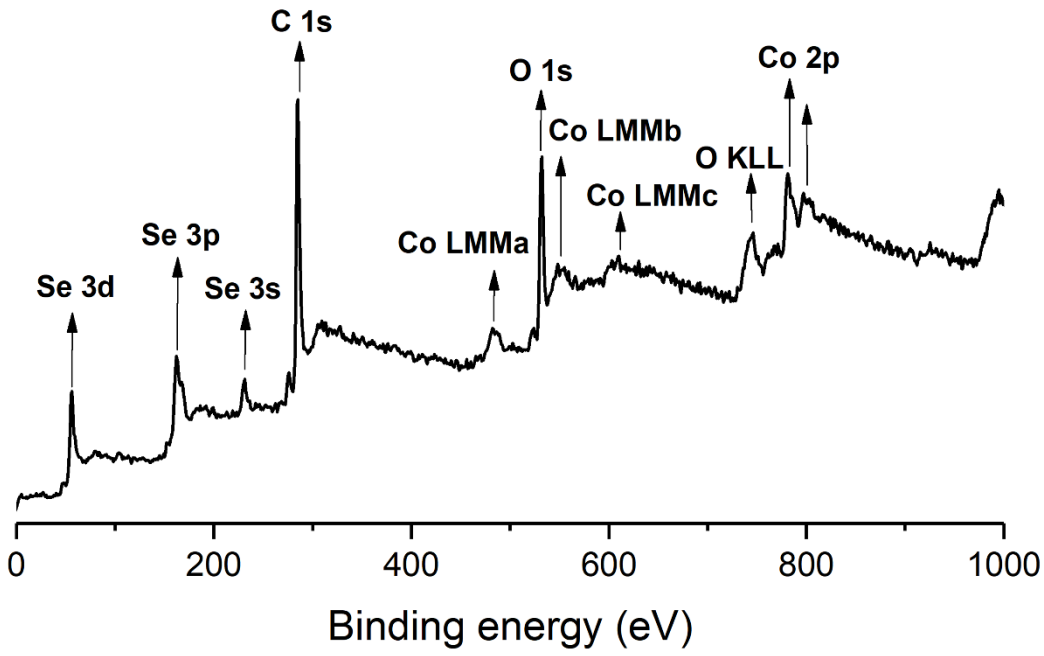

Figure S10. Full XPS spectra of Co-TPHS. (related to Figure 3)

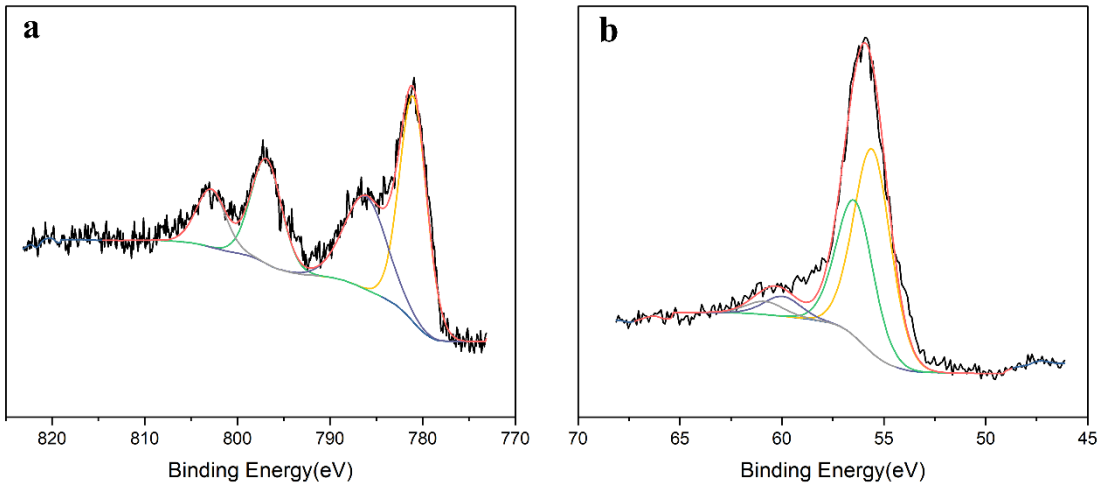

Figure S11. XPS analysis of Co-TPHS. (a) Co 2p and (b) Se 3d. (related to Figure 3)

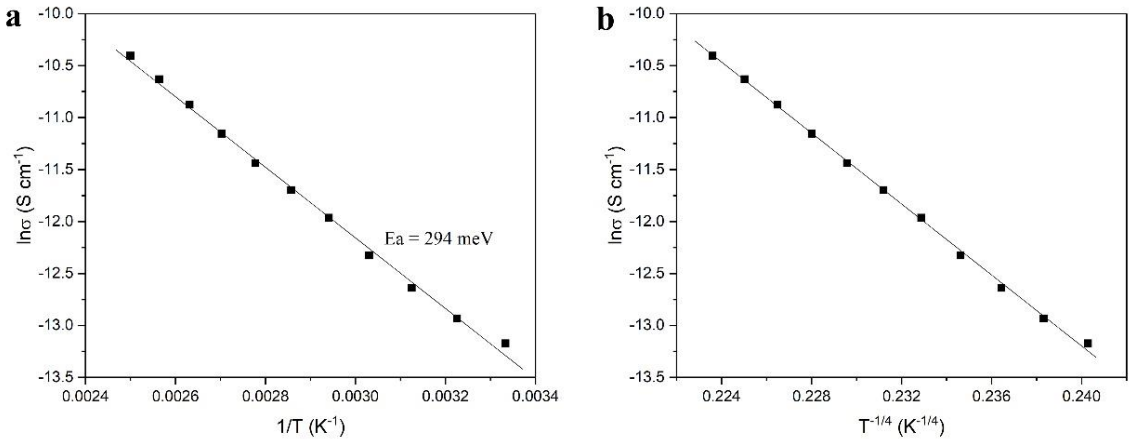

Figure S12. a) Plots of lnσ versus 1/T of Co-TPHS. b) Dependence of lnσ versus $T^{-1/4}$. (related to Figure 5)

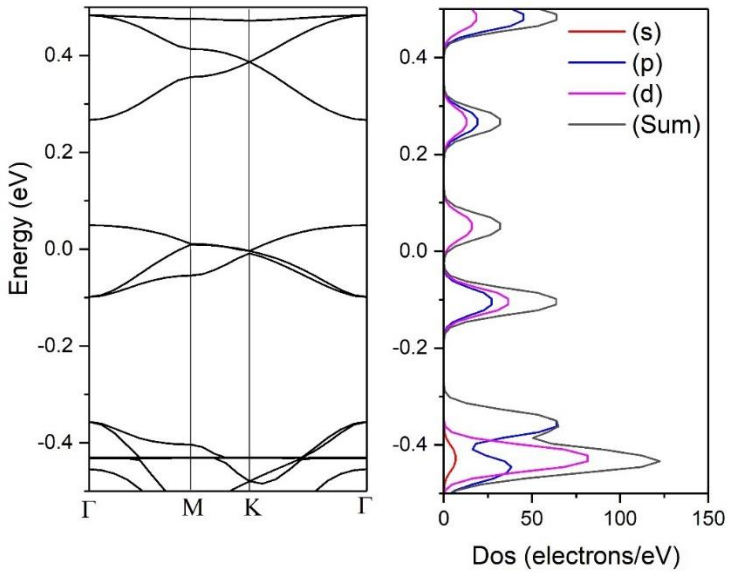

Figure S13. Band structure and density of state (DOS) of the monolayer of Co-TPHS complex calculated at PBE level. K point Γ=(0,0,0); K=(-0.333,0.667,0.000); M=(0.000,0.500,0.000). The Fermi level is at zero. (related to Figure 5)

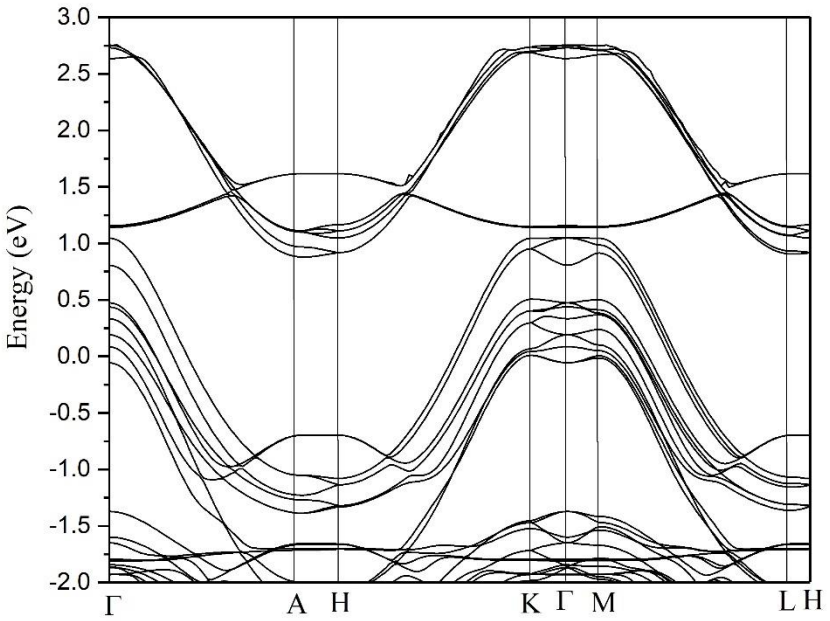

Figure S14. Band structure of the bulk crystal of eclipsed AA stacking Co-TPHS complex calculated at PBE level. K point Γ=(0,0,0); A=(0.000,0.000,0.500); H=(0.333,0.667,0.500); K=(-0.333,0.667,0.000); M=(0.000,0.500,0.000); L=(0.000,0.500,0.500). The Fermi level is at zero. (related to Figure 5)

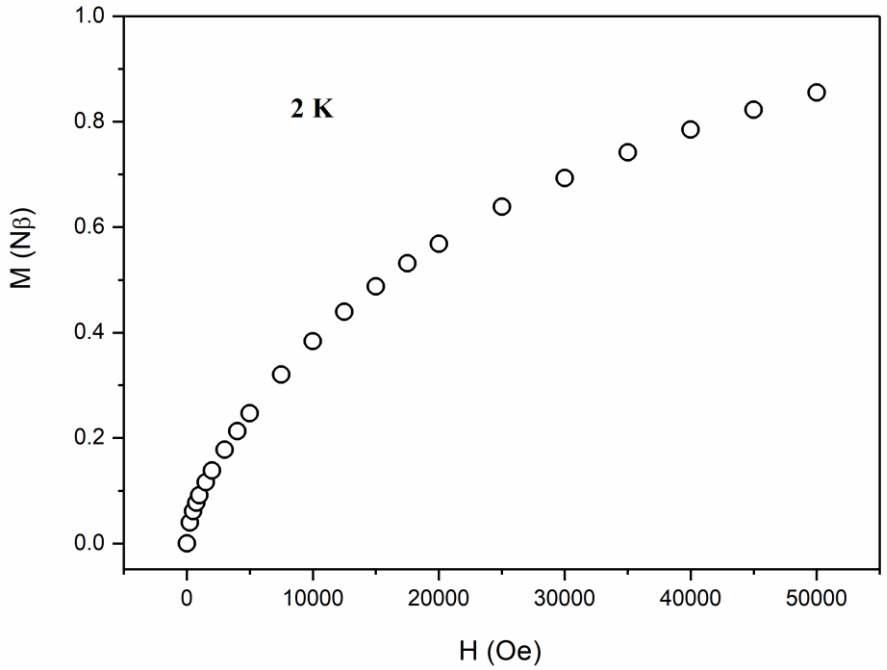

Figure S15. The field dependent magnetization at 2 K for Co-TPHS. (related to Figure 6)

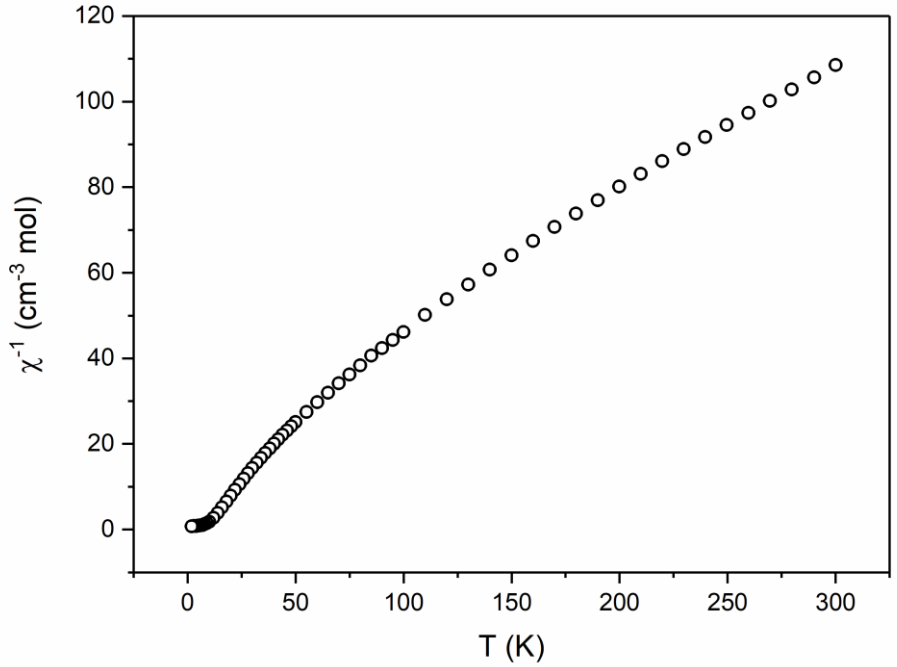

Figure S16. Plot of χ^{-1} versus T of Co-TPHS under 1k Oe field. (related to Figure 6)

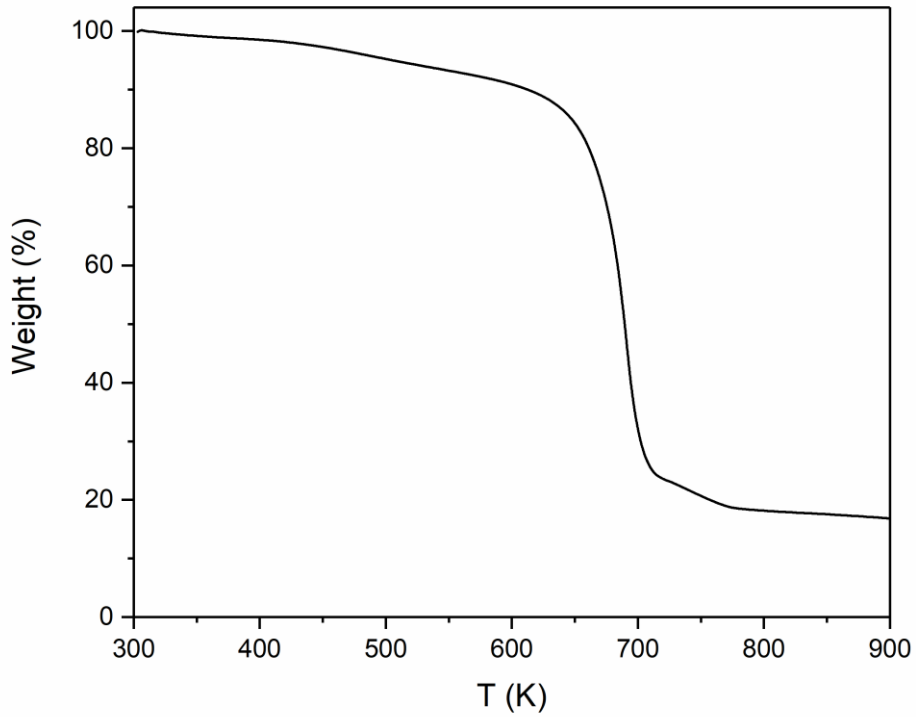

Figure S17. TGA curves of Co-TPHS. (related to Figure 6)

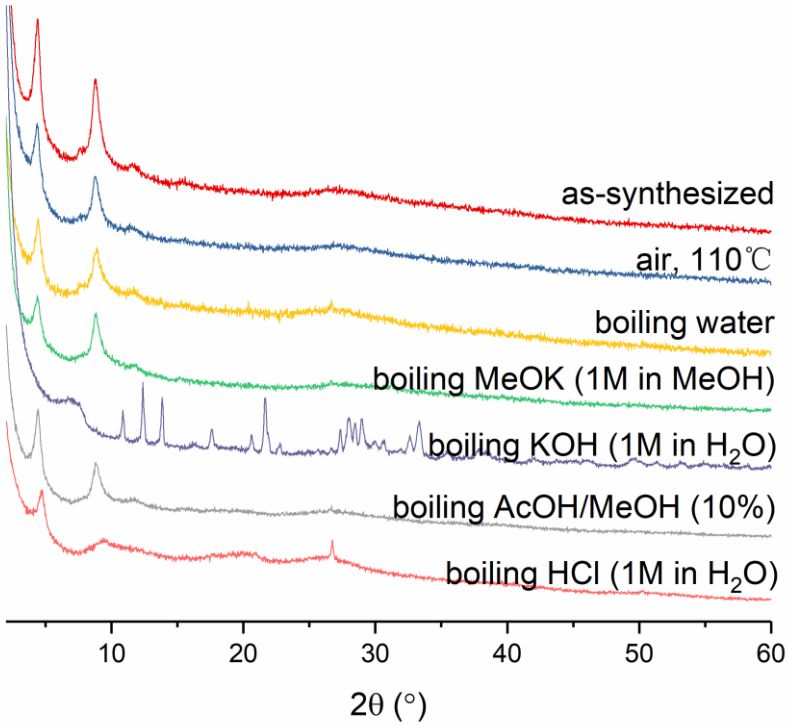

Figure S18. PXRD patterns of Co-TPHS after the treatment in different thermal or chemical environment for 24h. (related to Figure 3)

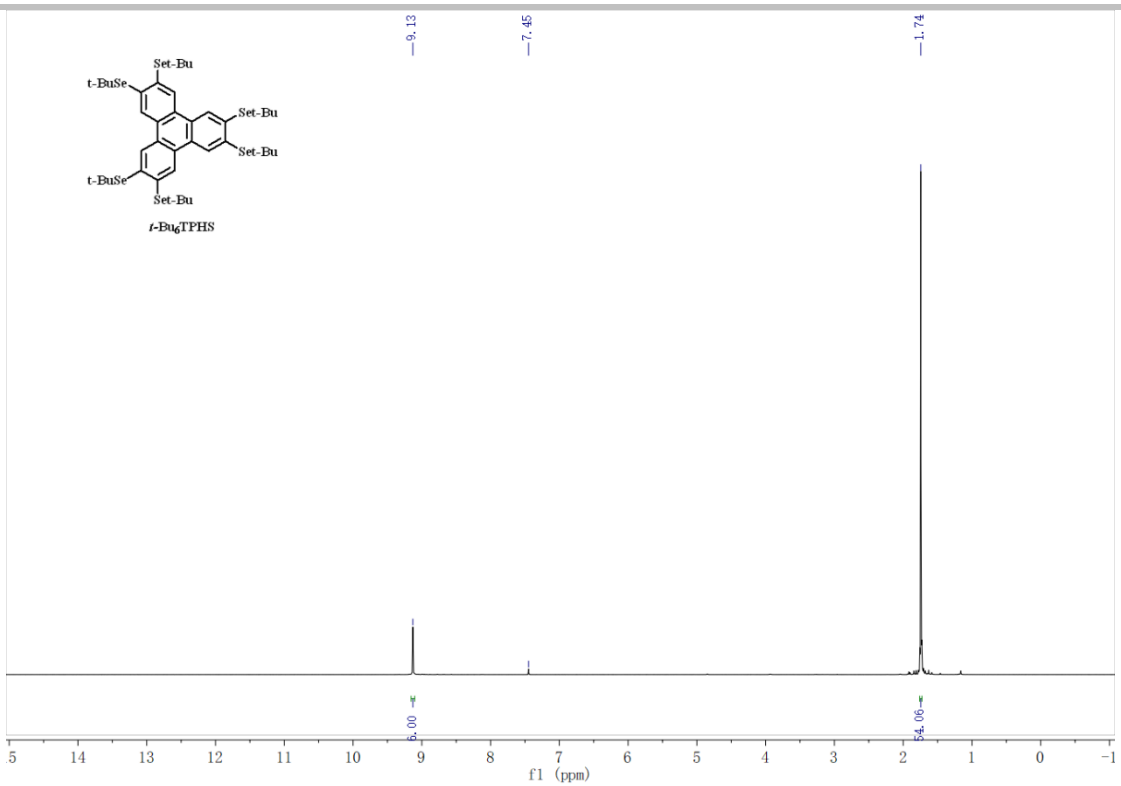

Figure S19. ^{1}H-NMR (400MHz, 298K, $CDCl_3$) spectrum of (*t*-Bu)$_6$TPHS. (related to Figure 1)

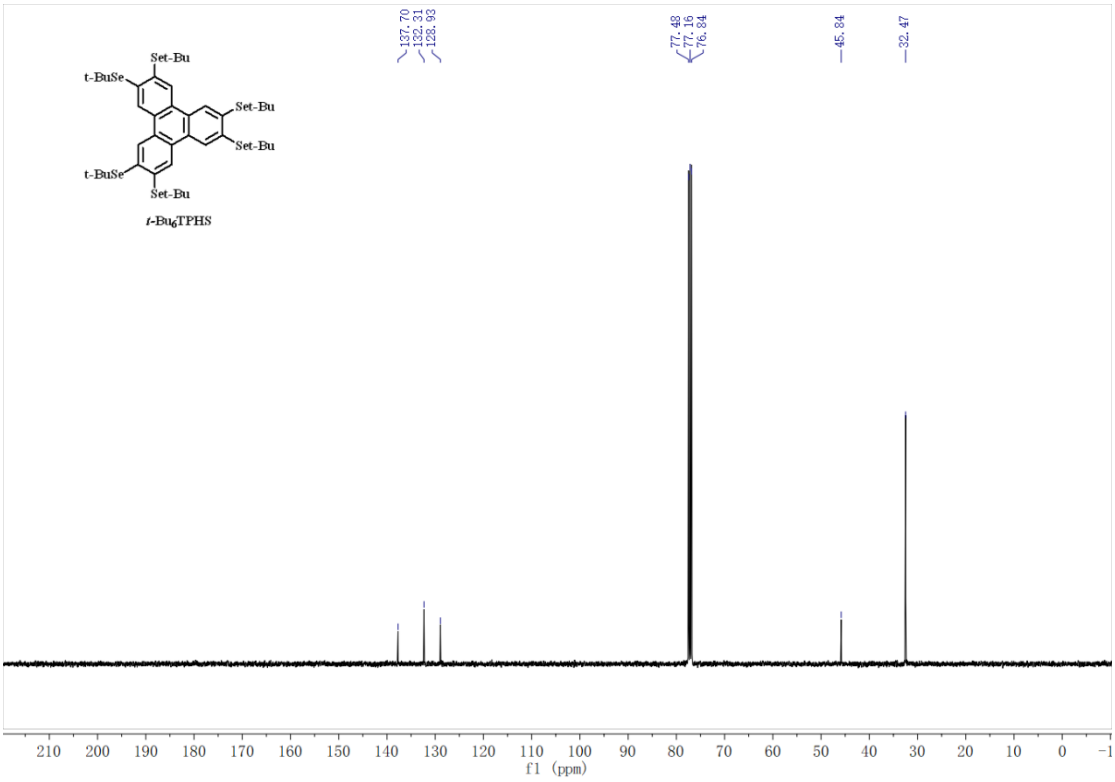

Figure S20. ^{13}C-NMR (400MHz, 298K, $CDCl_3$) spectrum of (*t*-Bu)$_6$TPHS. (related to Figure 1)

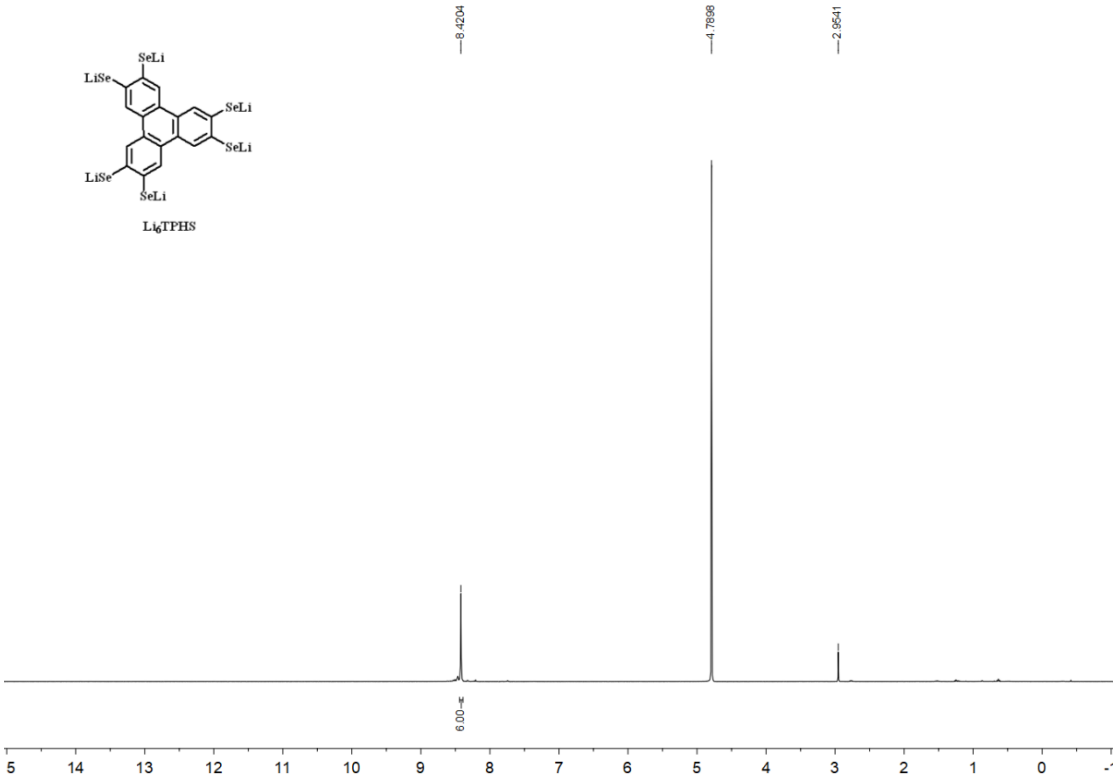

Figure S21. ^{1}H-NMR (400MHz, 298K, LiOD/D_2O) spectrum of $(Li)_6$TPHS which was obtained from the reaction of $(BBr)_3$TPHS and LiOD in D_2O. (related to Figure 1)

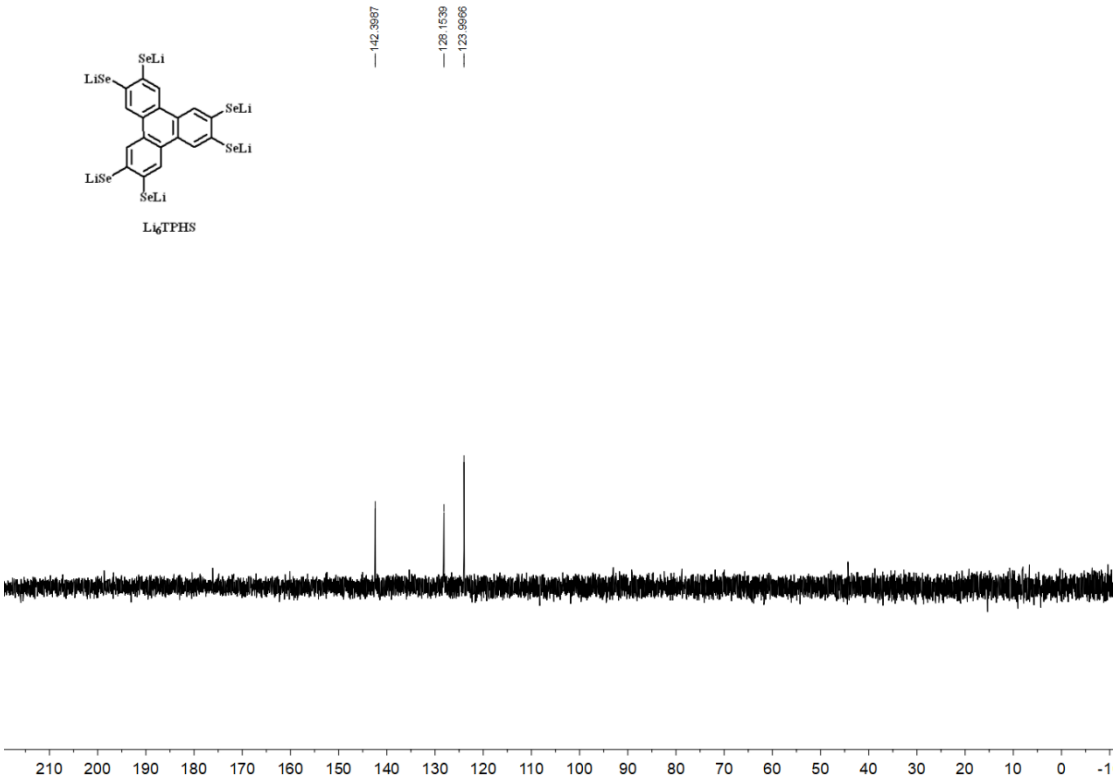

Figure S22. ^{13}C-NMR (400MHz, 298K, LiOD/D_2O) spectrum of $(Li)_6$TPHS which was obtained from the reaction of $(BBr)_3$TPHS and LiOD in D_2O. (related to Figure 1)

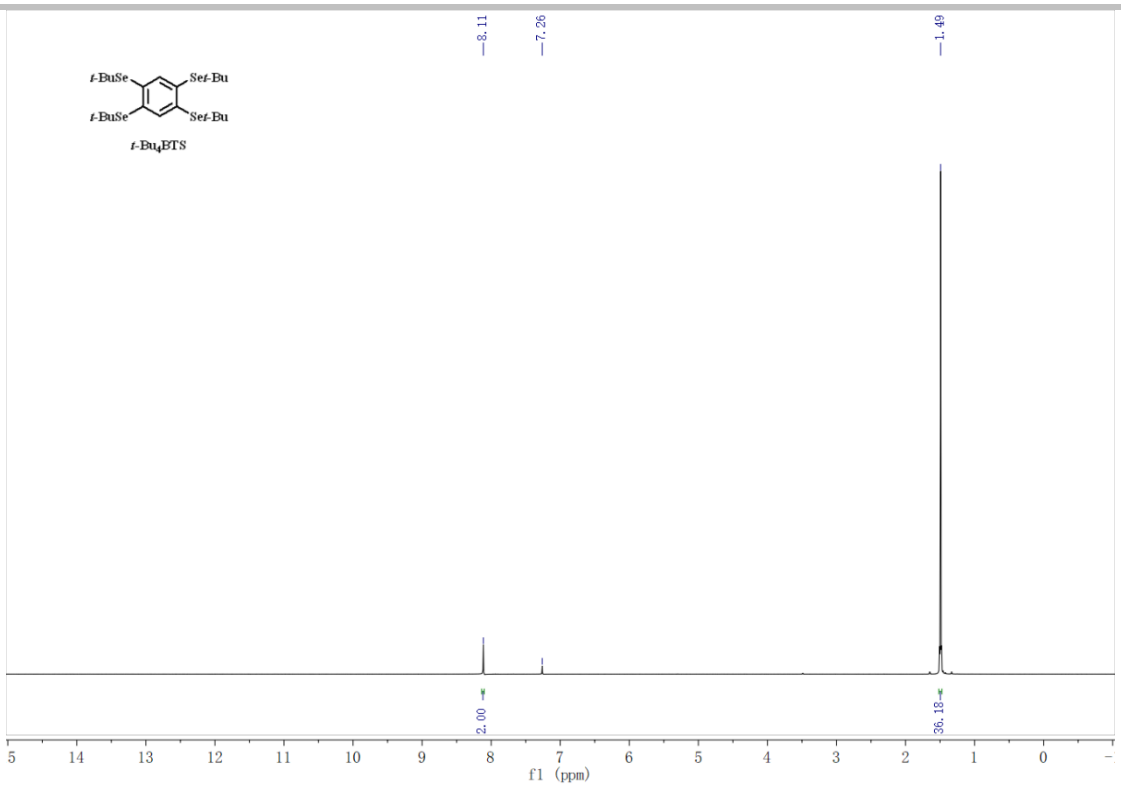

Figure S23. ^{1}H-NMR (400MHz, 298K, $CDCl_3$) spectrum of $(BBr)_2BTS$. (related to Figure 2)

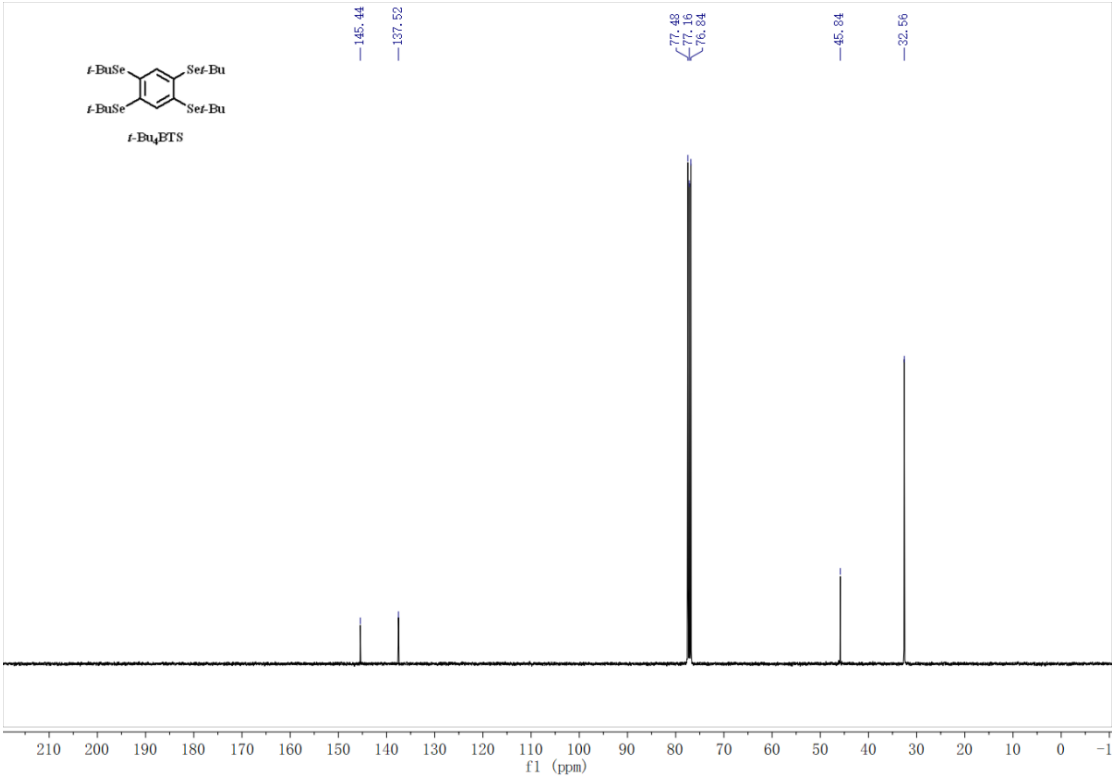

Figure S24. ^{13}C-NMR (400MHz, 298K, $CDCl_3$) spectrum of $(BBr)_2BTS$. (related to Figure 2)

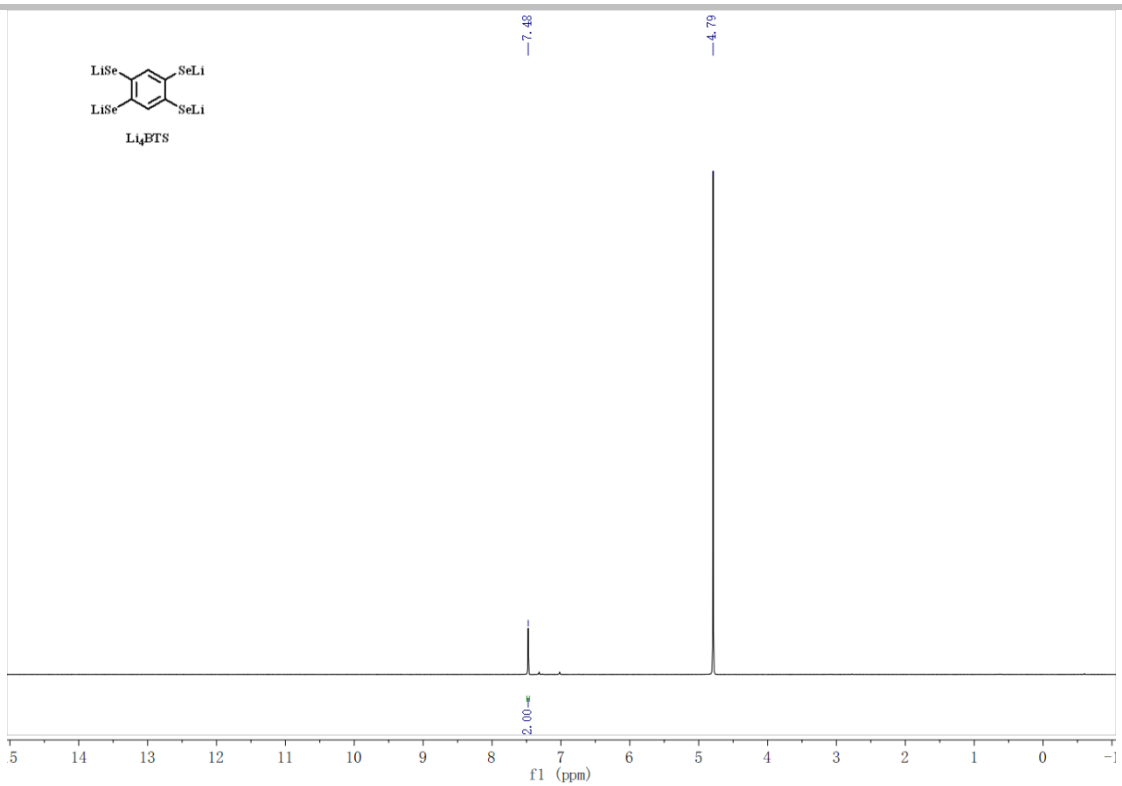

Figure S25. ^{1}H-NMR (400MHz, 298K, LiOD/D_2O) spectrum of $(Li)_4BTS$ which was obtained from the reaction of $(BBr)_2BTS$ and LiOD in D_2O. (related to Figure 2)

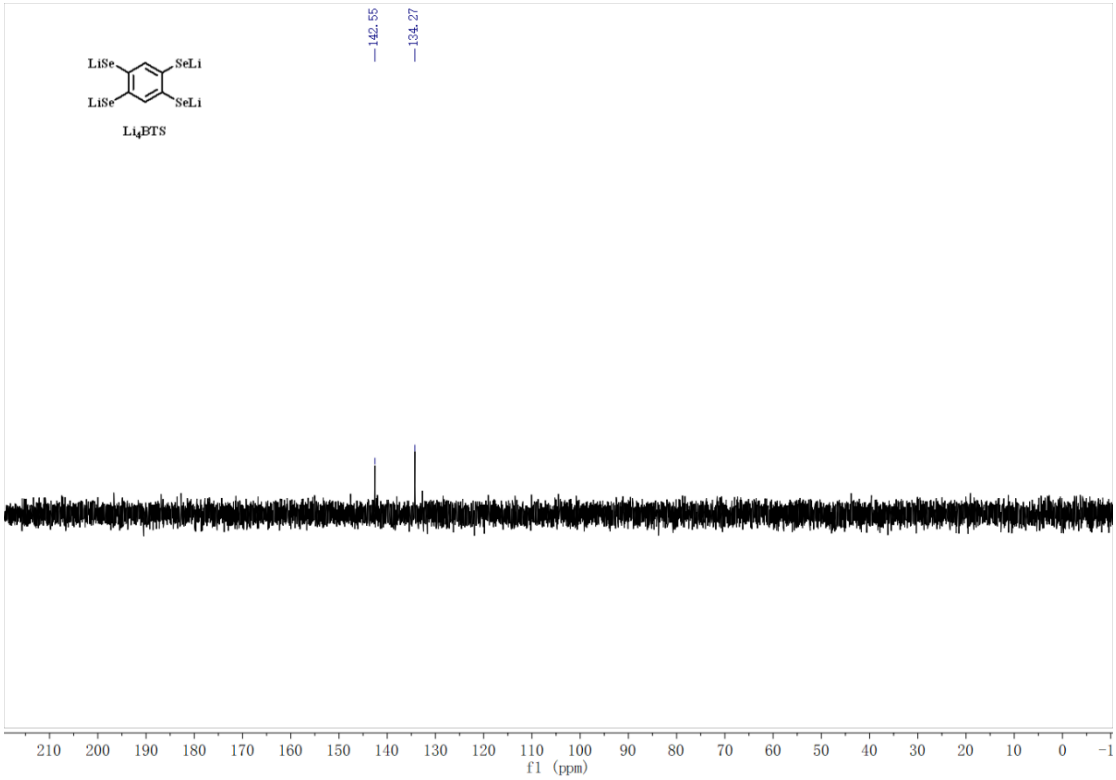

Figure S26. ^{13}C-NMR (400MHz, 298K, LiOD/D_2O) spectrum of $(Li)_4BTS$ which was obtained from the reaction of $(BBr)_2BTS$ and LiOD in D_2O. (related to Figure 2)

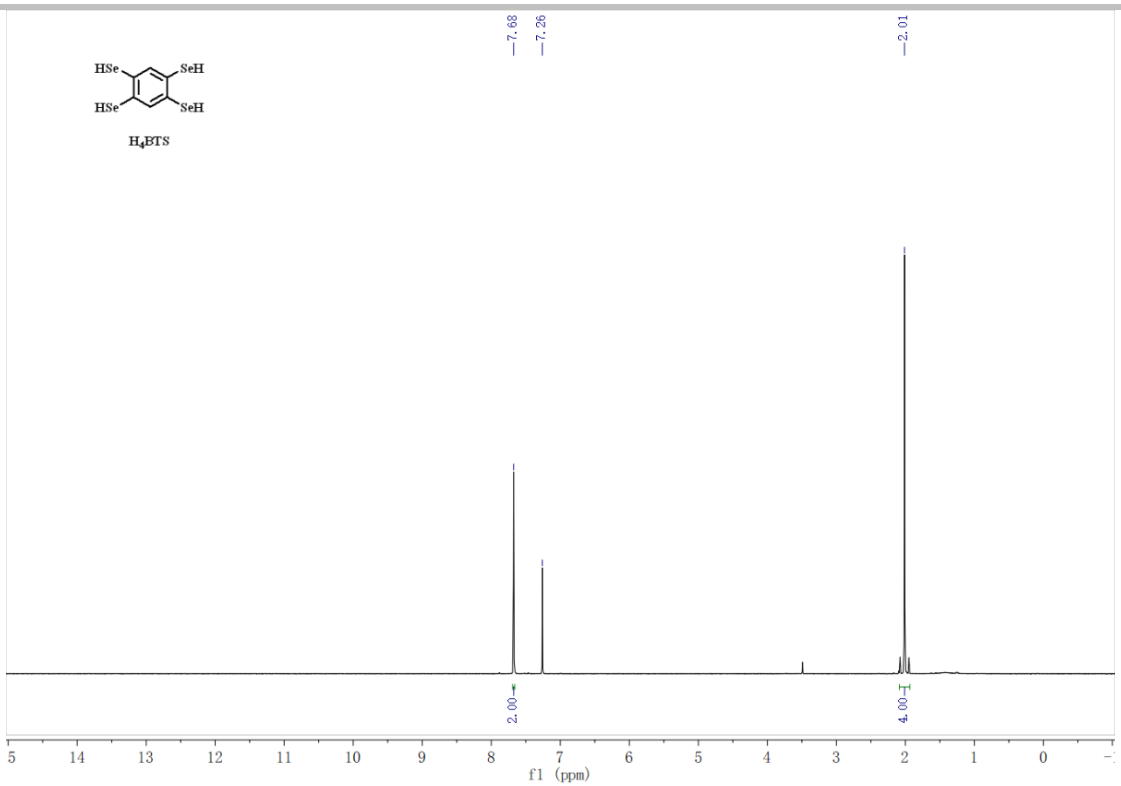

Figure S27. ^{1}H-NMR (400MHz, 298K, $CDCl_3$) spectrum of H_4BTS. (related to Figure 2)

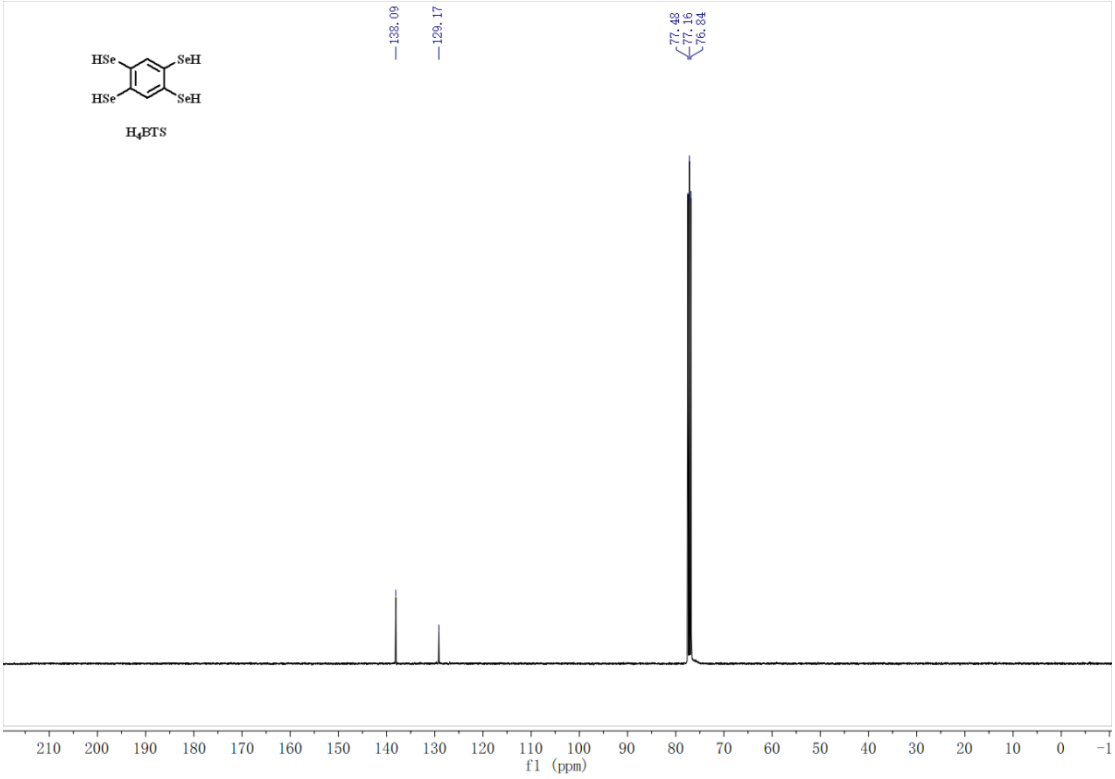

Figure S28. ^{13}C-NMR (400MHz, 298K, $CDCl_3$) spectrum of H_4BTS. (related to Figure 2)

References

Turner, D. L. & Vaid, T. P. 2012. Synthesis of protected benzenepolyselenols. *J Org Chem,* 77**,** 9397-400.

Yatabe, T., Harbison, M. A., Brand, J. D., Wagner, M., Müllen, K., Samorí, P. & Rabe, J. P. 2000. Extended triphenylenes: synthesis, mesomorphic properties and molecularly resolved scanning tunneling microscopy images of hexakis(dialkoxyphenyl)triphenylenes and dodeca(alkoxy)tris(triphenylenylene)s. *Journal of Materials Chemistry,* 10**,** 1519-1525.